Resource

SOURCE DATA TRANSPARENT PROCESS

THE EMBO JOURNAL

Single-cell transcriptomics of LepR-positive skeletal cells reveals heterogeneous stress-dependent stem and progenitor pools

Chunyang Mo[1,†], Jingxin Guo[2,3,†], Jiachen Qin[1], Xiaoying Zhang[1], Yuxi Sun[4], Hanjing Wei[1], Dandan Cao[1], Yiying Zhang[1], Chengchen Zhao[1], Yanhong Xiong[1], Yong Zhang[1], Yao Sun[5], Li Shen[2,3,6,*] & Rui Yue[1,7,**]

Abstract

Leptin receptor (LepR)-positive cells are key components of the bone marrow hematopoietic microenvironment, and highly enrich skeletal stem and progenitor cells that maintain homeostasis of the adult skeleton. However, the heterogeneity and lineage hierarchy within this population has been elusive. Using genetic lineage tracing and single-cell RNA sequencing, we found that Lepr-Cre labels most bone marrow stromal cells and osteogenic lineage cells in adult long bones. Integrated analysis of Lepr-Cre-traced cells under homeostatic and stress conditions revealed dynamic changes of the adipogenic, osteogenic, and periosteal lineages. Importantly, we discovered a Notch3$^+$ bone marrow sub-population that is slow-cycling and closely associated with the vasculatures, as well as key transcriptional networks promoting osteo-chondrogenic differentiation. We also identified a Sca-1$^+$ periosteal sub-population with high clonogenic activity but limited osteo-chondrogenic potential. Together, we mapped the transcriptomic landscape of adult LepR$^+$ stem and progenitor cells and uncovered cellular and molecular mechanisms underlying their maintenance and lineage specification.

Keywords bone marrow stromal cells; LepR$^+$ cells; periosteum; single-cell RNA-seq; skeletal stem/progenitor cells

Subject Categories Development; Methods & Resources; Stem Cells & Regenerative Medicine

DOI 10.15252/embj.2021108415 | Received 6 April 2021 | Revised 17 November 2021 | Accepted 18 November 2021 | Published online 27 December 2021

The EMBO Journal (2022) 41: e108415

See also: **J Sun & MB Greenblatt** (February 2022)

Introduction

Multiple waves of stem and progenitor cells contribute to the development, maintenance, and remodeling of the skeleton (Takashima *et al*, 2007; Nagoshi *et al*, 2008; Morikawa *et al*, 2009; Maes *et al*, 2010; Park *et al*, 2012; Liu *et al*, 2013; Isern *et al*, 2014; Mizoguchi *et al*, 2014; Ono *et al*, 2014; Yang *et al*, 2014; Zhou *et al*, 2014a, 2014b). Our previous study showed that LepR marks skeletal stem and progenitor cells (SSPCs) in the adult bone marrow (Zhou *et al*, 2014a), which largely overlap with Cxcl12-abundant reticular (CAR) cells (Omatsu *et al*, 2010) and Nestin-GFP^{low} cells (Mendez-Ferrer *et al*, 2010; Kunisaki *et al*, 2013). Genetic lineage tracing by Lepr-Cre labels bone marrow stromal cells (BMSCs) in early postnatal mice that generate most osteoblasts (OBs) and adipocytes during aging or after irradiation (Zhou *et al*, 2014a). They also generate chondrocytes after bone fracture or articular injury (Mizoguchi *et al*, 2014; Zhou *et al*, 2014a). Conditional deletion of *LepR* from limb bones led to increased osteogenesis and decreased adipogenesis, suggesting that LepR regulates SSPC maintenance and differentiation (Yue *et al*, 2016). LepR$^+$ cells localize in the perivascular region of the adult bone marrow, which produces a repertoire of extracellular matrix proteins and osteogenic factors to promote bone formation (Yue *et al*, 2016). LepR$^+$ cells also secrete high levels of hematopoietic stem cell (HSC) maintenance factors to create the hematopoietic microenvironment (Ding *et al*, 2012; Greenbaum *et al*, 2013; Zhou *et al*, 2014a; Crane *et al*, 2017), highlighting their pivotal roles in orchestrating hematopoiesis and osteogenesis. In addition to LepR$^+$/CAR/Nestin-GFP^{low} cells, Pdgfrα$^+$Sca-1$^+$ (PαS) cells (Morikawa *et al*, 2009), NG2$^+$ cells (Kunisaki *et al*, 2013), and

1 Institute for Regenerative Medicine, Shanghai East Hospital, Frontier Science Center for Stem Cell Research, Shanghai Key Laboratory of Signaling and Disease Research, School of Life Sciences and Technology, Tongji University, Shanghai, China
2 MOE Key Laboratory of Biosystems Homeostasis & Protection and Zhejiang Provincial Key Laboratory for Cancer Molecular Cell Biology, Life Sciences Institute, Zhejiang University, Hangzhou, China
3 Department of Orthopedics Surgery, 2nd Affiliated Hospital, School of Medicine, Zhejiang University, Hangzhou, China
4 Department of Cardiology, Shanghai Tenth People's Hospital, Tongji University School of Medicine, Shanghai, China
5 Department of Implantology, School & Hospital of Stomatology, Shanghai Engineering Research Center of Tooth Restoration and Regeneration, Tongji University, Shanghai, China
6 Hangzhou Innovation Center, Zhejiang University, Hangzhou, China
7 Shanghai Institute of Stem Cell Research and Clinical Translation, Shanghai, China
*Correspondening author. Tel: +86 571 88981751; E-mail: li_shen@zju.edu.cn
**Correspondening author. Tel: +86 21 65983623; E-mail: ryue@tongji.edu.cn
†These authors contributed equally to this work

non-myelinating Schwann cells (Yamazaki *et al*, 2011) were also proposed as critical components of the HSC niche. However, the heterogeneity of LepR$^+$ cells and the extent to which they overlap with other HSC niche cells need to be addressed at single-cell resolution.

By high-throughput single-cell RNA sequencing (scRNA-seq), we and others have mapped the mouse bone marrow stroma in an unbiased way (Han *et al*, 2018; Baryawno *et al*, 2019; Baccin *et al*, 2020). However, transcriptomic profiling of unfractionated cells resulted in low resolution of SSPCs due to over-representation of osteoblasts, chondrocytes, vascular endothelial cells, and fibroblasts (Han *et al*, 2018; Baryawno *et al*, 2019). scRNA-seq analysis of Col2-Cre-traced cells in young and aged mice revealed a marrow adipogenic lineage precursor (MALP) population (Zhong *et al*, 2020), which highly resembles LepR$^+$ cells (Zhou *et al*, 2014a). However, since Col2-Cre also labels large numbers of chondrocytes and osteogenic lineage cells, the heterogeneity within MALPs was not resolved (Zhong *et al*, 2020). Another scRNA-seq study analyzed Lepr-Cre-traced cells in steady state and 5-FU-treated mouse bone marrow (Tikhonova *et al*, 2019). Unfortunately, bone fragments containing large amounts of SSPCs in the endosteum and periosteum were excluded from this study, therefore, limited heterogeneity was observed within Lepr-Cre-traced cells (Tikhonova *et al*, 2019). Given that LepR$^+$ cells are largely quiescent under steady state (Zhou *et al*, 2014a), integrated analysis of stress conditions that efficiently drive their differentiation along the adipogenic, osteogenic, or chondrogenic lineages could help reveal the intrinsic heterogeneity within LepR$^+$ cells in adult mice.

Apart from the bone marrow and endosteum, SSPCs also exist in the periosteum to promote bone formation and fracture repair (Duchamp de Lageneste *et al*, 2018). Periosteal stem cells (PSCs) were identified in both long bones and calvaria, which mediate intramembranous ossification under steady state and repair fractures by endochondral ossification (Debnath *et al*, 2018). Mx1$^+$αSMA$^+$ periosteal SSCs (p-SSCs) were also shown to regulate fracture healing in a CCR5-dependent manner (Ortinau *et al*, 2019). Interestingly, Lepr-Cre labels a sub-population of periosteal cells, which are expanded in response to bone fracture (Mizoguchi *et al*, 2014). However, the cellular heterogeneity and functional divergence within periosteal Lepr-Cre$^+$ cells remain elusive. In this study, we performed single-cell transcriptomic profiling and functional analysis of SSPCs in adult long bones by focusing on Lepr-Cre-traced cells. Integrated analysis under homeostatic and stress conditions (e.g., aging, rosiglitazone feeding, irradiation, and bone fracture) revealed novel cellular and molecular mechanisms underlying SSPC maintenance and lineage specification.

Results

Mapping Prrx1-Cre- and Lepr-Cre-traced cells under homeostatic condition

During long bone development, *Prrx1* is highly expressed by limb bud mesenchymal progenitors (Cserjesi *et al*, 1992). Therefore, genetic lineage tracing by Prrx1-Cre labels all skeletal lineage cells in long bones, including SSPCs, osteoblasts, osteocytes, chondrocytes, and adipocytes (Logan *et al*, 2002). To resolve the heterogeneity within SSPCs, we crossed *Prrx1-Cre* or *Lepr-Cre* mice with a *loxp-STOP-loxp-tdTomato* reporter line to perform genetic lineage tracing (*Prrx1-Cre; tdTomato* and *Lepr-Cre; tdTomato*, respectively), and compared the extent to which Prrx1-Cre$^+$ and Lepr-Cre$^+$ cells overlap in adult long bones. We also crossed a *Col2.3-GFP* reporter line with *Prrx1-Cre; tdTomato* mice (*Prrx1-Cre; tdTomato; Col2.3-GFP*) to exclude most OBs traced by Prrx1-Cre during development. Lived non-hematopoietic and non-endothelial tdTomato$^+$ GFP$^-$ cells (for Prrx1-Cre), or tdTomato$^+$ cells (for Lepr-Cre) were sorted from the bone marrows and bone fragments of 8-week-old male mice by flow cytometry (Figs 1A and EV1A), followed by scRNA-seq on 10X Genomics platform (Fig 1A). After quality control, we obtained 4,170 and 3,050 single cells from *Prrx1-Cre; tdTomato; Col2.3-GFP* and *Lepr-Cre; tdTomato* mice, respectively.

After correcting batch effects, we performed integrated analysis of Prrx1-Cre- and Lepr-Cre-traced cells, which revealed nine subsets using non-linear dimensionality reduction with t-distributed stochastic neighbor embedding (tSNE) (Figs 1B and EV1B). Specifically, we identified subsets including BMSCs (clusters 0, 1, 5, and 6, expressing *Lepr and Kitl*) (Ding *et al*, 2012; Zhou *et al*, 2014a), pro/pre-OBs (cluster 2, expressing *Alpl* and *Wif1*) (Delgado-Calle *et al*, 2011; Baker *et al*, 2015), OBs (cluster 7, expressing *Col1a1* and *Bglap2*) (Kratochwil *et al*, 1993; Li *et al*, 2010), chondrocytes (cluster 4, expressing *Col2a1 and Acan*) (Doege *et al*, 1991; Chan *et al*, 1995), and αSMA$^+$ cells (cluster 8, expressing *Acta2* and *Myh11*; Fig 1C and D). We also identified a subset that highly expressed *Col3a1* (Fig 1D). RNA *in situ* hybridization showed that Col3a1$^+$ cells are mainly localized in the periosteal regions of femur metaphysis and diaphysis (Fig 1E). Interestingly, periosteal cells (cluster 3), chondrocytes (cluster 4), and αSMA$^+$ cells (cluster 8) were mainly derived from Prrx1-Cre (Figs 1F and EV1C). In contrast, BMSCs (clusters 0, 1, 5, 6) and osteogenic lineage cells (cluster 2, 7) were traced by both Cre lines, suggesting that Lepr-Cre could reliably label SSPCs and their descendants in adult mice. Consistent with the fact that Col2.3-GFP labels most but not all OBs in an age-dependent manner (Kalajzic *et al*, 2002), we could still observe an OB subset (cluster 7) within Prrx1-Cre$^+$ cells even after excluding Col2.3-GFP$^+$ cells (Fig 1B). We confirmed that most cells within this subset expressed *tdTomato* but not *GFP* transcripts (Fig EV1D). Pseudotime analysis by RNA velocity (Bergen *et al*, 2020) showed an osteogenic differentiation trajectory from BMSCs (cluster 0) to pro/pre-OBs (cluster 2) and OBs (cluster 7; Fig 1G).

We also systematically analyzed the expression of well-known SSPC markers in our dataset (Fig EV1E). *Cxcl12* (Sugiyama *et al*, 2006), *Pdgfra* (Morikawa *et al*, 2009), *Pdgfrb* (Koide *et al*, 2007), and *Grem1* (Worthley *et al*, 2015) were highly expressed in BMSCs (Fig EV1E). *CD105* (Chan *et al*, 2009) is also expressed in BMSCs, although at a lower level (Fig EV1E). *Itgav* (*CD51*) (Pinho *et al*, 2013) was highly expressed in pro/pre-OBs and OBs, while *CD24a* (Rodeheffer *et al*, 2008; Ambrosi *et al*, 2017), *NG2* (*Cspg4*) (Kunisaki *et al*, 2013), and *CD73* (*Nt5e*) (Breitbach *et al*, 2018) were highly expressed in chondrocytes (Fig EV1E). Interestingly, *Ly6a* (*Sca-1*) (Morikawa *et al*, 2009) was highly expressed in periosteal cells, while the human BMSC marker *Mcam* (*CD146*) (Sacchetti *et al*, 2007) was highly expressed in αSMA$^+$ cells (Fig EV1E). CD200 (Chan *et al*, 2015) showed a broad distribution among BMSCs, OBs, chondrocytes, and αSMA$^+$ cells (Fig EV1E). In contrast, *Nes* (*Nestin*) (Mendez-Ferrer *et al*, 2010) was expressed in very few cells among all subsets (Fig EV1E).

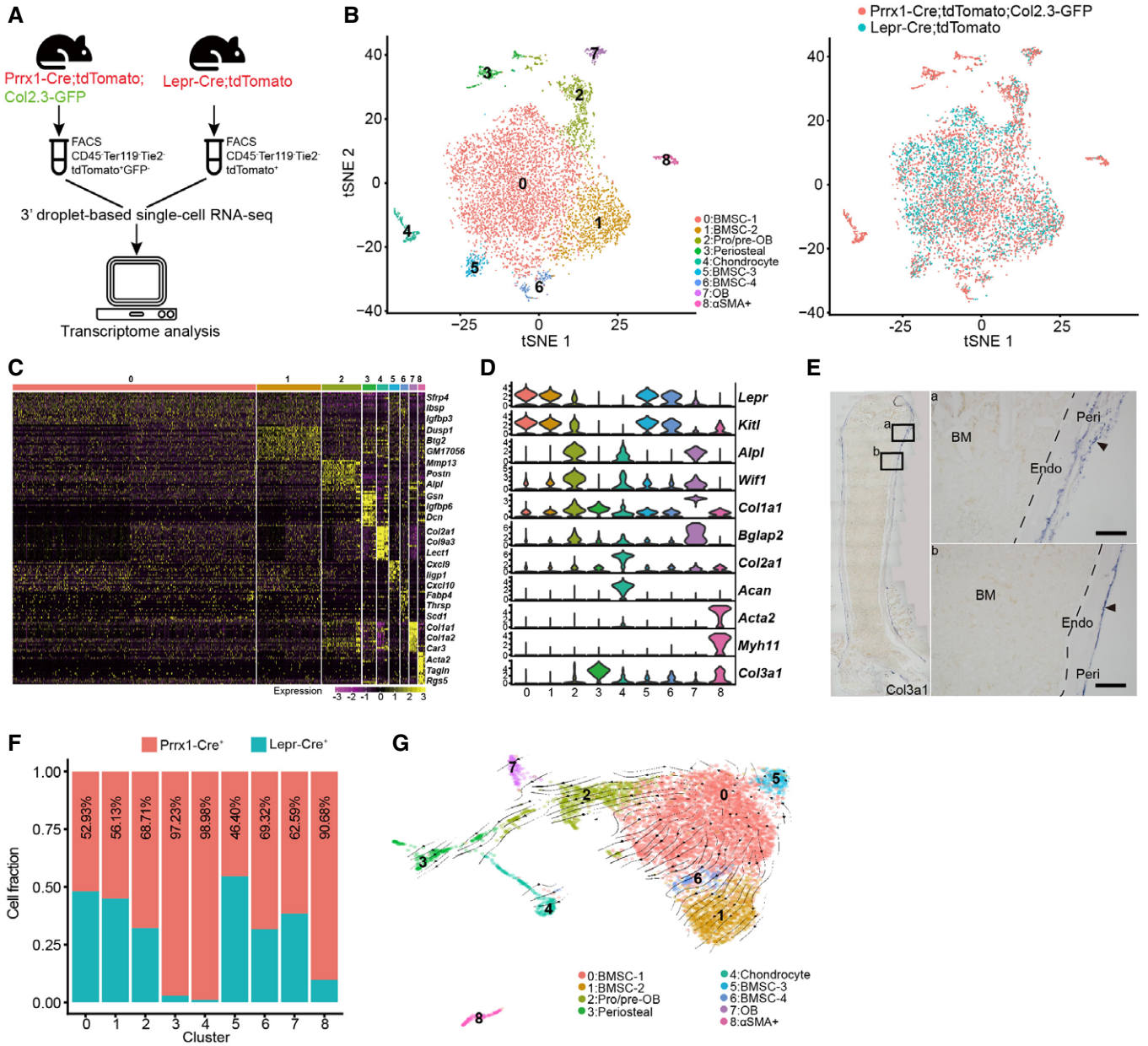

Figure 1. Comparison of Prrx1-Cre- and Lepr-Cre-traced cells in adult long bones.

A Schematic overview of the scRNA-seq workflow.

B t-SNE plots showing integrated analysis of Prrx1-Cre- (8-week-old mice, n = 3 males) and Lepr-Cre-traced (8-week-old mice, n = 4 males) cells. Cells were colored by clusters (left) or samples (right). Top 20 PCs were chosen for the clustering.

C Heatmap showing the relative expression levels (row-wide Z score) of the 20 most significant markers for each cluster (rows) across cells in the 9 clusters (columns). Bars on the top were colored as in (B).

D Violin plots showing the expression of feature genes for each cluster.

E *In situ* hybridization of *Col3a1* on femur sections. *Col3a1* was expressed in the perichondral (a) and periosteal (b) regions, but not in the bone marrow. B: Bone; BM: Bone marrow; Peri: Periosteum; Endo: Endosteum. Scale bars are 100 μm. Arrowheads indicated the periosteum.

F Relative contribution to each cluster by Prrx1-Cre- and Lepr-Cre-traced cells after normalization to total cells (4,170 cells in Prrx1-Cre, 3,050 cells in Lepr-Cre).

G UMAP plot showing the inferred trajectories by RNA velocity analysis.

Integrated analysis of Lepr-Cre-traced cells under homeostatic and stress conditions

We then focused on *Lepr-Cre; tdTomato* mice to analyze the lineage specification of SSPCs under adipogenic or osteo-chondrogenic stress conditions (Fig 2A). Rosiglitazone is a potent agonist of Pparγ, which has been shown to promote marrow fat accumulation after prolonged feeding (Ackert-Bicknell *et al*, 2009; Horowitz *et al*, 2017; Farrell *et al*, 2021). Aging also promotes marrow fat accumulation, while irradiation leads to accelerated adipogenic and

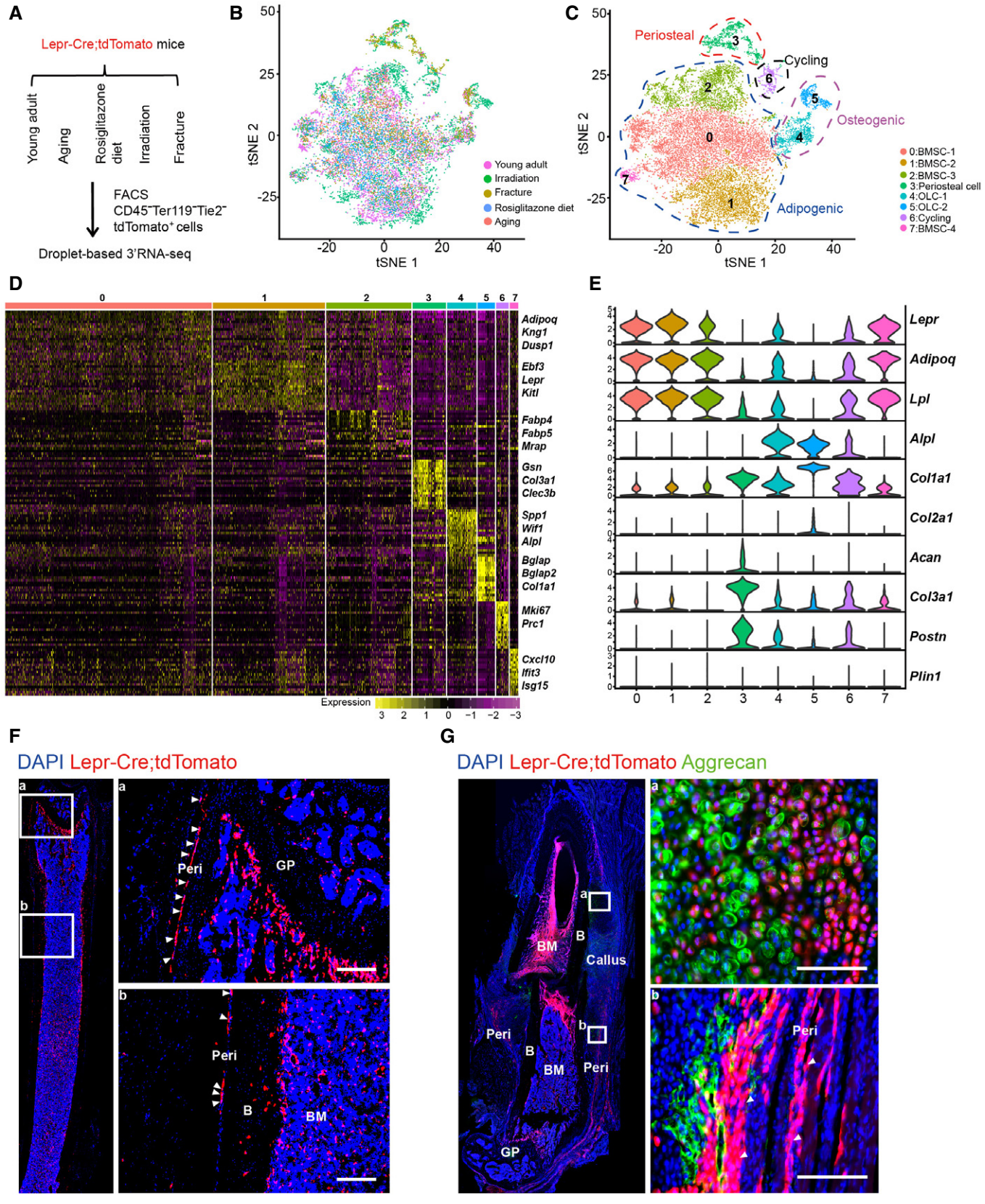

Figure 2.

Figure 2. Integrated analysis of Lepr-Cre-traced cells under homeostatic and stress conditions.

A Schematic overview of scRNA-seq strategies in *Lepr-Cre; tdTomato* mice. Young adult: 8-week-old mice (4 males and 2 females); Aging: 12-month-old mice (4 females); Rosiglitazone diet: 10-week-old mice (feeding started at 5 weeks old, 2 females); Irradiation: 8-week-old mice (sub-lethally irradiated at 7 weeks old, 2 males and 2 females); Fracture: 8-week-old mice (femur fractured at 7 weeks old, 2 males and 2 females).

B, C t-SNE plots showing 17,224 CD45$^-$ Ter119$^-$ Tie2$^-$ tdTomato$^+$ single cells from all 5 conditions. Cells are colored by conditions (B) or clustering (C). The adipogenic, osteogenic, periosteal, and cycling cells were highlighted by dotted lines in (C). Top 20 PCs were chosen for the clustering.

D Heatmap showing the relative expression levels (row-wide Z score) of the 20 most significant markers for each cluster (rows) across cells in the 8 clusters (columns). Bars on the top were colored as in (C).

E Violin plots showing the expression of feature genes for each cluster.

F Immunofluorescent images of the distal femur in 8-week-old *Lepr-Cre; tdTomato* mice. Arrowheads indicated tdTomato$^+$ periosteal cells. Two representative periosteal regions were magnified (a and b). GP: Growth plate. B: Bone. BM: Bone marrow. Peri: Periosteum. Scale bars are 100 μm.

G Immunofluorescent images of the distal femur in 8-week-old *Lepr-Cre; tdTomato* mice 7 days after fracture. Aggrecan (green), tdTomato (red), DAPI (blue). Arrowheads indicated tdTomato$^+$ periosteal cells. Two representative regions were magnified (a and b). Scale bars are 100 μm.

osteogenic differentiation by LepR$^+$ BMSCs (Zhou *et al*, 2014a). In contrast, bone fracture drives SSPC differentiation along the osteochondral lineage to promote endochondral ossification and bone remodeling (Worthley *et al*, 2015). After quality control and filtering, we obtained 5,022 cells from 8-week-old mice (young adult, males and females), 2,619 cells from 12-month-old mice (aging, females), 2,545 cells from 10-week-old mice on rosiglitazone diet for 5 weeks (fed at 5 weeks old, females), 4,514 cells from sub-lethally irradiated 8-week-old mice (irradiated at 7 weeks old, males and females), and 2,524 cells from the fractured femurs of 8-week-old mice (unilaterally fractured at 7 weeks old, males and females; Fig 2A).

After correcting batch effects, integrated analysis revealed eight subsets based on marker expressions (Figs 2B and C and EV2C), which could be grouped into three lineages: (i) Adipogenic lineage cells (clusters 0, 1, 2, and 7) that expressed *Lepr*, *Adipoq*, and *Lpl* (Kindblom *et al*, 2005); (ii) Osteogenic lineage cells (OLCs) that expressed *Alpl* and *Col1a1* (clusters 4 and 5); (iii) Periosteal lineage cells that expressed *Col3a1* and *Postn* (Duchamp de Lageneste *et al*, 2018) (cluster 3), as well as *Acan* (Fig 2 D and E); and (iv) Cycling cells that expressed *Mki67* (Tikhonova *et al*, 2019) (cluster 6), which were mainly induced by irradiation (Fig EV2C and D). Similar cell clustering was observed after segregating females (expressing *Xist*, *Esr1,* or *Esr2*) and males (expressing *Ddx3y*, *Eif2s3y*, *Kdm5d,* or *Uty*) cells (Skelly *et al*, 2018; Fig EV2A and B).

Although only a few Lepr-Cre$^+$ periosteal cells could be detected in young adults (Figs 2F and EV2C and D), they were expanded after bone fracture (Figs 2G and EV2C–E) and irradiation (Fig EV2C and D). As compared to young adults, the frequency of OLCs (clusters 4 and 5) was higher after bone fracture and irradiation, and lower under adipogenic stresses (Fig EV2C and D). The number of bone marrow adipocytes was dramatically increased in aged mice, as well as after rosiglitazone diet feeding and sub-lethal irradiation (Fig EV2F). Notably, the adipogenic subsets (clusters 0, 1, 2, and 7) highly expressed *Adipoq* and *Lpl* (Fig 2E), but not the mature adipocyte marker *Perilipin* (*Plin1*) (Fig 2E). This indicated that they represent Lepr-Cre$^+$ BMSCs with adipogenic potential, but not terminally differentiated bone marrow adipocytes containing large lipid droplets, which could not be sorted by flow cytometrically for scRNA-seq analysis. As far as we are concerned, these adipogenic lineage cells are similar to previously reported Adipo-CAR cells (Baccin *et al*, 2020) and MALPs (Zhong *et al*, 2020).

Next, we dissected the heterogeneity and lineage hierarchy within each lineage by integrated analysis of the homeostatic and stress conditions.

Heterogeneity analysis within the adipogenic lineage cells

The adipogenic lineage cells were sub-divided into six subsets (Figs 3 A and EV3A). Cluster 1 expressed the highest level of *Lepr*, *Kitl*, and *Cxcl12*, as well as angiogenesis-related genes such as *Vegfa*, *Notch3,* and *Col4a1* (Domenga *et al*, 2004; Van Agtmael *et al*, 2010; Chen *et al*, 2019; Fig 3B). Cell cycle analysis revealed that cluster 1 contains more cells in the G1 phase and less cells in the S phase (Fig 3C). Consistent with this, bromodeoxyuridine (BrdU) incorporation analysis in 8-week-old *Lepr-Cre; tdTomato* mice showed fewer Lepr-Cre$^+$Notch3$^+$ cells in the S phase as compared to Lepr-Cre$^+$Notch3$^-$ cells (Fig 3D). Immunostaining on femur sections showed that Lepr-Cre$^+$Notch3$^+$ BMSCs represented adventitial cells closely associated with the vasculatures (Fig 3E and F), including sinusoids (Fig 3Ea), arterioles (Fig 3Eb), and arteries (Fig 3Ec), while Lepr-Cre$^+$Notch3$^-$ BMSCs represented reticular cells located in between vasculatures (Fig 3Ed).

To functionally test whether vasculature association regulates cell cycle and Notch signaling in BMSCs, we performed 3D culture of primary BMSCs with or without bone marrow endothelial cells (ECs) in 4% gelatin methacryloyl (GelMA) hydrogels (Fig 3G). RNA-seq and qPCR analyses revealed that co-culture with bone marrow ECs significantly increased *Notch3* and *Hes1* expression, and significantly decreased *Cdk6* expression in BMSCs (Figs 3H and I, and Fig EV3E). Flow cytometry analysis showed significantly increased frequency of Notch3$^+$ cells in Lepr-Cre$^+$ BMSCs co-cultured with ECs (Fig EV3C and D). BrdU incorporation analysis showed fewer Lepr-Cre$^+$Notch3$^+$ cells in S phase as compared to Lepr-Cre$^+$Notch3$^-$ cells during *ex vivo* culture (Fig 3J). Gene ontology (GO) and KEGG pathway analyses showed significant up-regulation of genes related to Notch signaling pathway (Fig 3K and L), while genes related to ossification, MAPK signaling, cell cycle, and TGF-b signaling pathways were significantly down-regulated (Fig EV3F and G). Consistent with the *in vivo* data (Fig 3E), immunostaining in the 3D co-culture system showed Lepr-Cre$^+$Notch3$^+$ BMSCs closely associated with ECs (Fig 3M and N). Thus, we identified a Notch3$^+$ BMSC subpopulation that corresponds to adventitial cells, which are maintained in a slow cycling state by ECs.

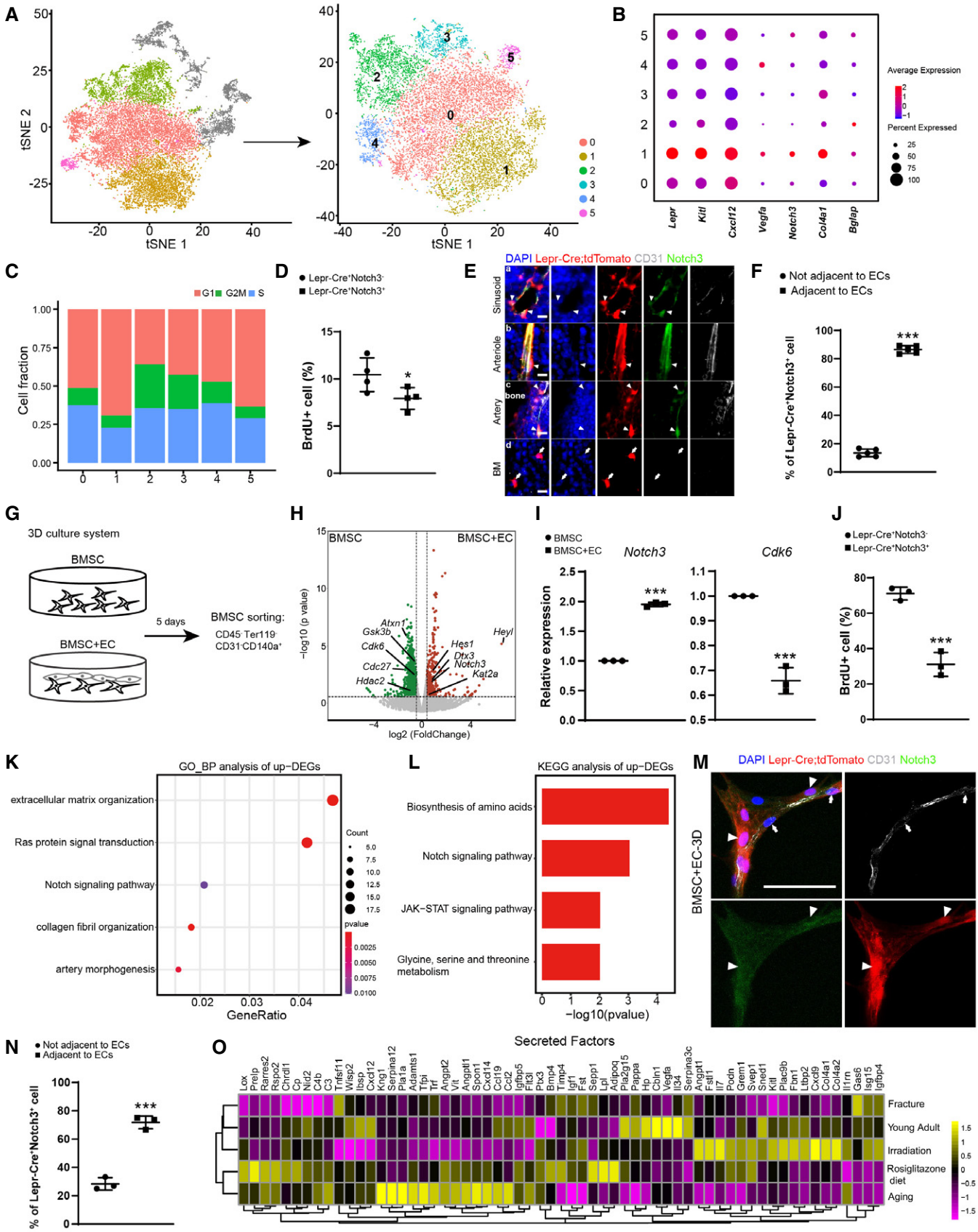

Figure 3.

Figure 3. Identification of a Notch3$^+$ sub-population within the adipogenic lineage cells.

A t-SNE plots showing the original (left) and re-clustered (right) adipogenic lineage cells by integrated analysis of homeostatic and stress conditions. Top 15 PCs were chosen for the clustering.
B Dot plots showing the gene expression patterns of selected genes in each cluster.
C Stacked bar charts showing the cell cycle status in all clusters.
D Flow cytometry analysis of BrdU incorporation in uncultured Lepr-Cre$^+$Notch3$^{+/-}$ BMSCs (n = 4 independent experiments). Eight-week-old *Lepr-Cre; tdTomato* mice were given a single intraperitoneal injection of BrdU (100 mg/kg body mass) and maintained on 0.5 mg/ml of BrdU in the drinking water for 14 days.
E Immunofluorescent images of the distal femur in 8-week-old *Lepr-Cre; tdTomato* mice. Notch3 (green), tdTomato (red), CD31 (gray), DAPI (blue). Sinusoid (a), arteriole (b), artery (c), and avascular bone marrow (BM, d) regions are shown. Arrowheads indicated Notch3$^+$ tdTomato$^+$ adventitial cells closely associated with ECs. Arrows indicated Notch3$^-$ tdTomato$^+$ reticular cells in the bone marrow that were not associated with ECs. Scale bars are 10 μm.
F Localization quantification of Lepr-Cre$^+$Notch3$^+$ cells relative to bone marrow ECs (n = 5 biological replicates from three independent experiments). Cells within 5 μm diameter of ECs were considered adjacent.
G Graphical illustration of the 3D co-culture system.
H Volcano plot showing DEGs in the bulk RNA-seq analysis (n = 3 biological replicates). Green dots represent down-regulated genes. Red dots represent up-regulated genes.
I qPCR analysis of *Notch3* and *Cdk6* expression (n = 3 independent experiments).
J Flow cytometry analysis of BrdU incorporation in Lepr-Cre$^+$Notch3$^{+/-}$ BMSCs after 3D co-cultured with bone marrow ECs (n = 3 independent experiments). BrdU was administered at a final concentration of 10 μM from culture day 1 to day 5.
K, L GO terms (K) and KEGG pathways (L) enriched in up-regulated genes.
M Representative confocal images of BMSCs 3D co-cultured with bone marrow ECs. Z-stack projection is shown. Notch3 (green), tdTomato (red), CD31 (gray), DAPI (blue). Arrowheads indicated Notch3$^+$tdTomato$^+$ adventitial cells. Arrows indicated bone marrow ECs. Scale bar is 50 μm.
N Localization quantification of Lepr-Cre$^+$Notch3$^+$ cells relative to bone marrow ECs after 3D co-culture (n = 3 biological replicates from three independent experiments). Cells within 25 μm diameter of ECs were considered adjacent.
O Heatmap showing the average expression levels (column-wide Z score) of secreted factors with clustering.

Data information: All data represented Mean ± SD. The statistical significance of differences was analyzed by two-tailed unpaired Student's t-test. *P < 0.05, ***P < 0.001.

As compared to cluster 1, cluster 0 contains more cells in S phase (Fig 3C), which is sensitive to irradiation (Fig EV3A and B). Cluster 2 enriched ossification genes such as *Bglap* (Fig 3B), which was expanded after irradiation and fracture (Fig EV3A and B). In contrast, cluster 3 enriched adipocyte marker genes (Dataset EV2), which was expanded by irradiation (Fig EV3A and B). Clusters 4 and 5 enriched immediate early response genes and interferon-stimulated genes (ISGs; Dataset EV2), respectively, the frequency of which remain largely constant under homeostatic and stress conditions (Fig EV3A and B). We also analyzed the secretory profiles in the adipogenic lineage cells (Fig 3O). As compared to young mice, the HSC niche factors *Kitl* and *Cxcl12* were down-regulated in aged, rosiglitazone-fed, and fractured mice (Fig 3O), suggesting a compromised HSC niche. In contrast to *Cxcl12*, *Kitl* expression was increased after irradiation (Fig 3O), consistent with a previous study that bone marrow adipogenesis after irradiation could promote hematopoietic regeneration via Kitl secretion (Zhou *et al*, 2017). Interestingly, the secretory profiles of aged and rosiglitazone-fed mice clustered together, implicating Pparγ activation as a potential mechanism underlying bone marrow aging (Sadie-Van Gijsen *et al*, 2013).

Heterogeneity analysis within the osteogenic lineage cells

The osteogenic lineage cells were sub-divided into three subsets (Figs 4A and EV4A), including Pro-OBs (cluster 0), Pre-OB (cluster 1), and mature OB (cluster 2). Pseudotime analysis revealed an osteogenic differentiation continuum (Fig 4B). BMSC markers *Lepr*, *Kitl*, and *Ebf3* (Seike *et al*, 2018) were dramatically down-regulated following lineage commitment, while the osteogenic factors, such as *Spp1*, *Postn* and *Aspn*, were gradually up-regulated (Figs 4C and EV4B). As cells underwent terminal differentiation into mature OBs, they expressed the highest level of mineralization factors such as *Col1a1*, *Bglap*, and *Bglap2* (Figs 4C and EV4B). As compared to young adult mice, the frequency of mature OBs was lower in aged and rosiglitazone-fed mice, but much higher after bone fracture and irradiation (Fig 4D). Consistent with this, secreted bone matrix factors such as *Col1a1*, *Col1a2*, *Sparc*, and *Bglap* were down-regulated in aged and rosiglitazone-fed mice (Fig EV4C), and up-regulated after bone fracture and irradiation (Fig EV4C).

To explore gene regulatory networks (regulons) underlying lineage specification, we applied a single-cell regulatory network

Figure 4. Identification of candidate osteo-chondrogenic regulators promoting fracture repair.

A t-SNE plots showing the original (left) and re-clustered (right) osteogenic lineage cells by integrated analysis of homeostatic and stress conditions. Top 10 PCs were chosen for the clustering.
B Pseudotime analysis by Monocle 2. Arrow indicated inferred direction of the differentiation trajectory.
C Heatmap showing pseudotime-dependent gene expression. Bars on the top were colored as in (A). Representative genes are highlighted on both sides.
D Frequencies of different osteogenic clusters under homeostatic and stress conditions.
E Heatmap showing the AUC score of regulons enriched in each stress. Z-score (row scaling) was calculated. Representative regulons were highlighted on the right.
F Representative images of adipogenic, osteogenic and chondrogenic differentiation following shRNA knockdown in Lepr-Cre$^+$ BMSCs. Scale bars are 100 μm.
G qPCR analysis of the expression levels of *Pparg*, *Bglap,* and *Acan* in control or knockdown group (n = 3 independent experiments). The statistical significance of differences was analyzed by one-way ANOVAs with Tukey's multiple comparison tests. Data represented Mean ± SD. *P < 0.05, **P < 0.01, ***P < 0.001.

Source data are available online for this figure.

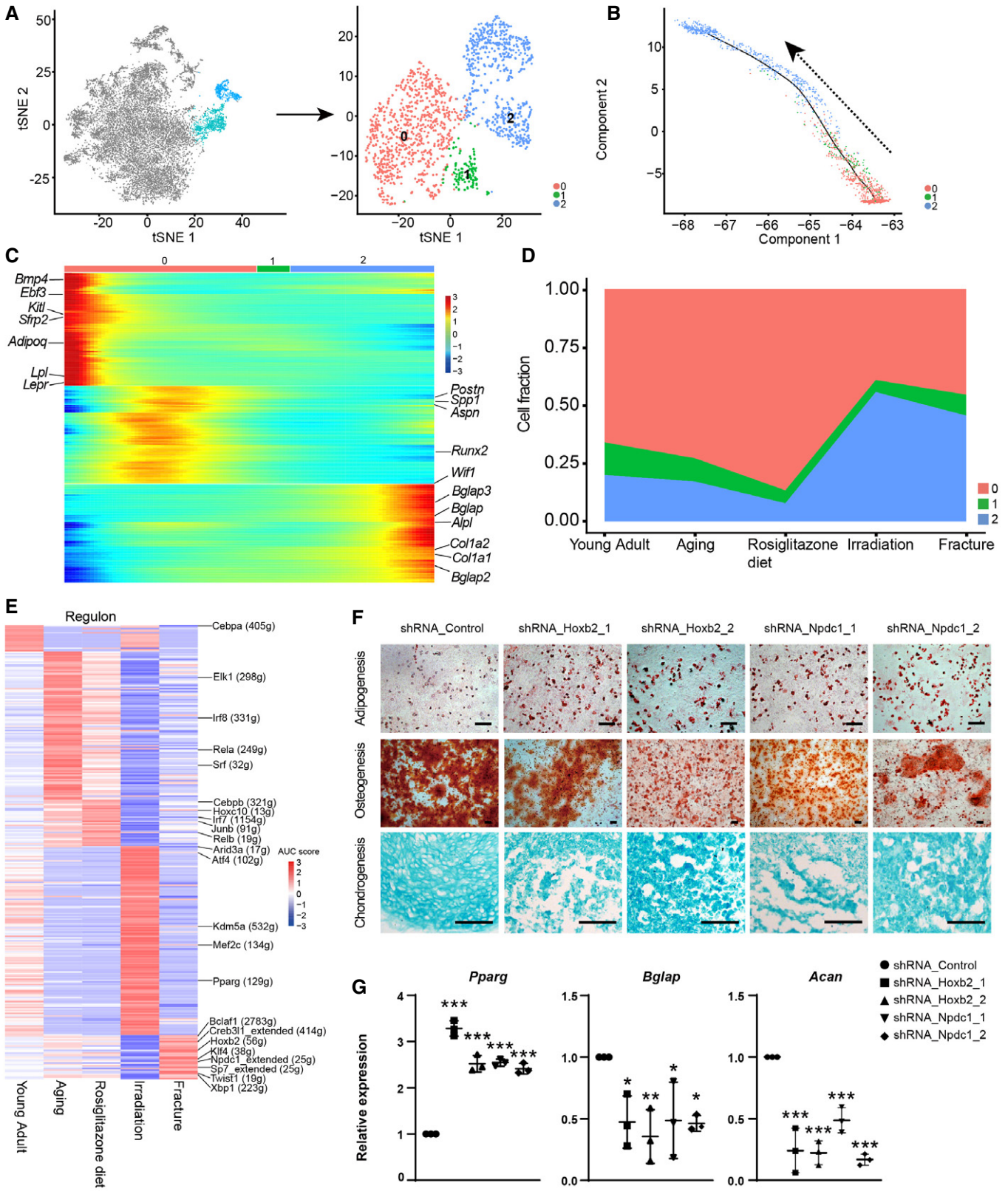

Figure 4.

inference and clustering (SCENIC) method to score the activity of regulons by an AUCell algorithm (AUC score), which reflects the co-expression of transcription factors (TFs) and their downstream target genes in each individual cell (Aibar *et al*, 2017). In addition to previously reported osteogenic regulons, such as Twist1, Atf4, Klf4, and Mef2c (Yang *et al*, 2004; Arnold *et al*, 2007; Miraoui *et al*, 2010; Kim *et al*, 2014), SCENIC analysis revealed that Hoxb2 and Npdc1 regulons were up-regulated after bone fracture (Fig 4E). To functionally test their roles in BMSC regulation, we knocked down *Hoxb2* and *Npdc1* in BMSCs by shRNA (Fig EV4D and E) and performed *in vitro* trilineage differentiation. Interestingly, knockdown of *Hoxb2* or *Npdc1* significantly increased adipogenic differentiation and decreased osteo-chondrogenic differentiation (Fig 4F), which was confirmed by qPCR analysis of the adipogenic (*Pparg*), osteogenic (*Bglap*), and chondrogenic (*Acan*) markers (Fig 4G). Renal subcapsular transplantation experiments showed that knockdown of *Hoxb2* or *Npdc1* impaired the osteo-chondrogenic differentiation of BMSCs *in vivo* (Fig EV4F and G). Thus, these data implicated Hoxb2 and Npdc1 as potential regulators of osteo-chondrogenic differentiation during fracture repair.

Heterogeneity analysis within the periosteal lineage cells

The periosteal lineage cells were expanded after irradiation and fracture (Fig EV5A), which were sub-divided into four subsets (Fig 5A). Importantly, all subsets expressed high levels of periosteal marker *Ctsk* (Debnath *et al*, 2018) but not *Lepr* (Fig 5B), suggesting that they correspond to CTSK$^+$ periosteal cells (Debnath *et al*, 2018). Cluster 0 highly expressed tenocyte marker *Tnmd* (Docheva *et al*, 2005), tissue remodeling factor *Ptx3* (Grcevic *et al*, 2018), as well as low levels of chondrocyte markers (Fig 5B). Cluster 1 highly expressed *Ly6a* (*Sca-1*) and *CD34* (Fig 5B). Cluster 2 highly expressed myofibroblast marker *Acta2* (*αSMA*; Roy *et al*, 2007; Fig 5B), reminiscent of the αSMA$^+$ p-SSCs (Ortinau *et al*, 2019). Cluster 3 highly expressed chondrocyte markers *Col2a1*, *Sox9,* and *Acan* (Fig 5B), as well as PSC markers (CD200$^+$CD105$^-$Thy1$^-$6C3$^-$; Debnath *et al*, 2018; Fig EV5B).

Pseudotime analysis showed that clusters 0 and 3 are closely related, while cluster 2 is intermediate between clusters 0 and 1 (Fig 5C). GO analysis revealed that clusters 0 and 3 enriched genes regulating skeletal development, and that clusters 1 and 2 enriched genes regulating angiogenesis (Fig 5D). Interestingly, SCENIC analysis showed enrichment of both chondrogenic (Sox4 and Sox9) and osteogenic (Twist and Sp7) regulons in cluster 3, while early-stage adipogenic regulon Cebpb was enriched in cluster 1 (Fig 5E), implicating their distinct differentiation potentials.

Although a similar Sca-1$^+$ subset (cluster 1 in this study) has been previously identified within CTSK$^+$ periosteal cells (Debnath *et al*, 2018), its localization, clonogenic and differentiation potentials remain elusive. To test this, we first analyzed the femur sections of 8-week-old *Lepr-Cre; tdTomato* mice (Fig 5F) and found Lepr-Cre$^+$ Sca-1$^+$ cells in the periosteum and cortical bones (Fig 5F). We then sorted Lepr-Cre$^+$ Sca-1$^+$ cells from the periosteum of unfractured femurs by flow cytometry (Fig 5G) and compared them with Lepr-Cre$^+$ and Lepr-Cre$^+$ Sca-1$^-$ cells by colony-forming unit-fibroblast (CFU-F) culture *ex vivo*. Lepr-Cre$^+$ Sca-1$^+$ cells formed significantly more colonies as compared to Lepr-Cre$^+$ and Lepr-Cre$^+$ Sca-1$^-$ cells (Fig 5H and I), while the colonies formed by Lepr-Cre$^+$ Sca-1$^-$ cells were significantly smaller than Lepr-Cre$^+$ and Lepr-Cre$^+$ Sca-1$^+$ cells (Fig 5J). We also sorted Lepr-Cre$^-$, Lepr-Cre$^-$ Sca-1$^+$, and Lepr-Cre$^-$ Sca-1$^-$ cells from the periosteum of unfractured femurs. Lepr-Cre$^-$ Sca-1$^-$ cells formed significantly fewer colonies with significantly smaller colony size as compared to Lepr-Cre$^-$ and Lepr-Cre$^-$ Sca-1$^+$ cells (Fig EV5C and D). Therefore, these data suggested that Sca-1 enriched CFU-F activity in both Lepr-Cre$^+$ and Lepr-Cre$^-$ fractions of the periosteum.

Next, we tested the tri-lineage differentiation potential of the periosteal subsets after *ex vivo* expansion. To our surprise, Lepr-Cre$^+$ Sca-1$^+$ cells underwent efficient adipogenic differentiation (Fig 6A and B), but limited osteo-chondrogenic differentiation (Fig 6C–F). In contrast, Lepr-Cre$^+$ Sca-1$^-$ cells showed significantly lower adipogenic differentiation (Fig 6A and B), and significantly higher osteo-chondrogenic differentiation as compared to Lepr-Cre$^+$ Sca-1$^+$ cells (Fig 6C–F). Similar results were also obtained in Lepr-Cre$^-$ fraction of the periosteum (Fig EV5E–J). Taken together, we found that Sca-1$^+$ periosteal cells enrich CFU-F activity but undergo limited osteo-chondrogenic differentiation.

Discussion

By comparing Prrx1-Cre- and Lepr-Cre-traced cells under homeostatic condition, we found that SSPC and osteogenic subsets were

Figure 5. Delineating the periosteal lineage cells.

A t-SNE plots showing the original (left) and re-clustered (right) periosteal lineage cells by integrated analysis of homeostatic and stress conditions. Top 10 PCs were chosen for the clustering.

B Violin plots showing the expression of feature genes for each cluster.

C Pseudotime trajectories of four clusters. Cells are colored as in (A).

D Dot plots showing the top5 GO terms enriched for each cluster.

E Heatmap showing the AUC score of regulons enriched in each cluster. Z-score (column scaling) was calculated. Representative regulons are highlighted on the top.

F Immunostaining of Sca-1 on femur sections of 8-week-old *Lepr-Cre; tdTomato* mice. Arrows indicate Sca-1$^+$ tdTomato$^+$ cells inside cortical bones of the femur diaphysis. Arrowheads indicate Sca-1$^+$ tdTomato$^+$ cells in the femur periosteum. B: Bone. BM: Bone marrow. Peri: Periosteum. Scale bar is 100 μm.

G Representative flow cytometry plots of long bone periosteum in 8-week-old *Lepr-Cre; tdTomato* mice. The percentage of DAPI$^-$ CD45$^-$ Ter119$^-$ Tie2$^-$ tdTomato$^+$ Sca-1$^{+/-}$ cells are shown.

H Representative CFU-F colony images. Two hundred DAPI$^-$ CD45$^-$ Ter119$^-$ Tie2$^-$ tdTomato$^+$ (Lepr-Cre$^+$), DAPI$^-$ CD45$^-$ Ter119$^-$ Tie2$^-$ tdTomato$^+$ Sca-1$^+$ (Lepr-Cre$^+$Sca-1$^+$), or DAPI$^-$ CD45$^-$ Ter119$^-$ Tie2$^-$ tdTomato$^+$ Sca-1$^-$ (Lepr-Cre$^+$ Sca-1$^-$) cells were sorted from the limb bone periosteum of *Lepr-Cre; tdTomato* mice and cultured for 8 days, followed by crystal violet staining.

I, J The average number of CFU-F colonies formed (I) and the average cell number per colony (J) are shown (n = 4 independent experiments). The statistical significance of differences was assessed using one-way ANOVAs with Tukey's multiple comparison tests. All data represented Mean ± SD. *P < 0.05, **P < 0.01, ***P < 0.001.

Source data are available online for this figure.

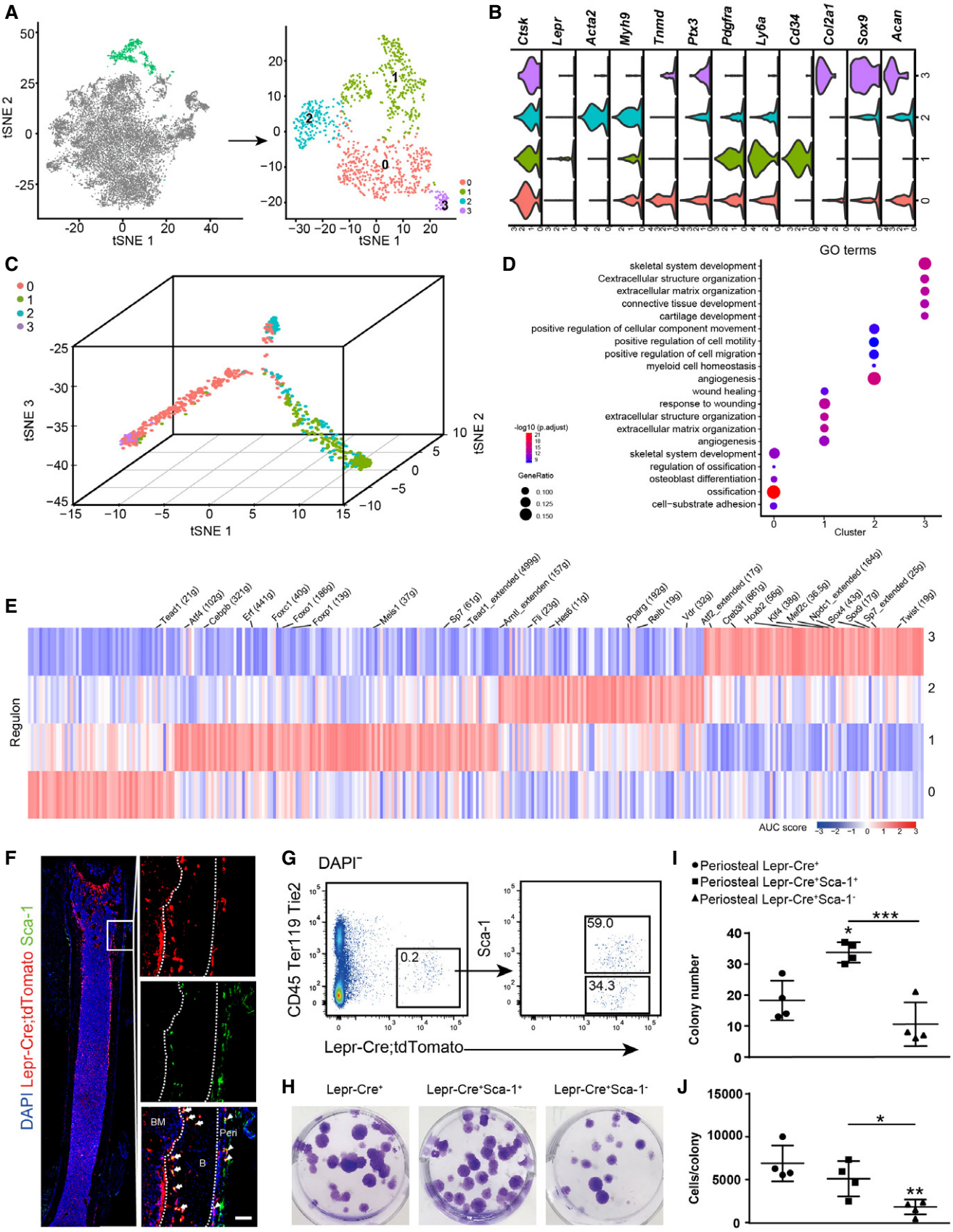

Figure 5.

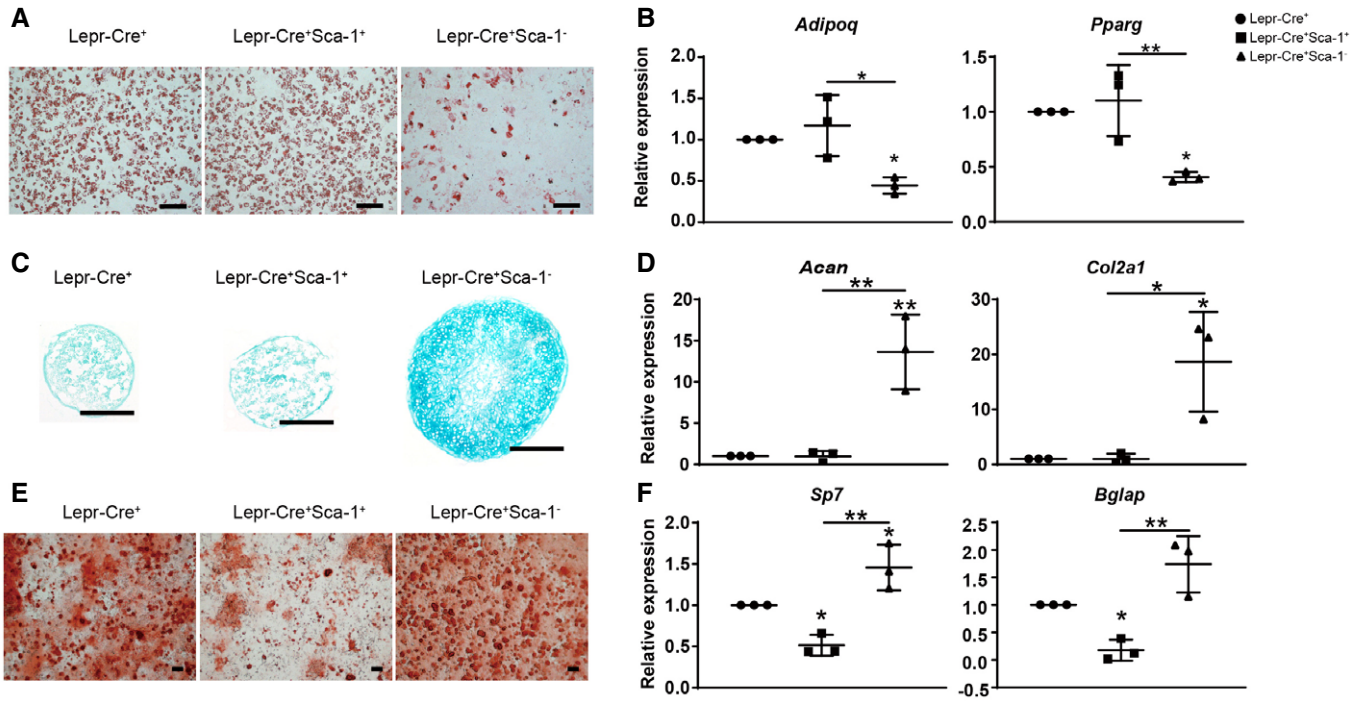

Figure 6. Functional analysis of the Sca-1$^+$ sub-population in the periosteum.

A, B Representative oil red staining after 7 days of adipogenic differentiation in Lepr-Cre$^+$ subsets (A) and qPCR analysis of *Adipoq* and *Pparg* expression (B) (n = 3 independent experiments). Scale bars are 100 μm.

C, D *In vitro* chondrogenic differentiation of sorted periosteal cells. Representative alcian blue staining after chondrogenic differentiation for 21 days and cryosection (C). Scale bars are 100 μm. Chondrogenic efficiencies were quantified by qPCR analysis of *Acan* and *Col2a1* expression (D) (n = 3 independent experiments).

E, F *In vitro* osteogenic differentiation of sorted periosteal cells. Representative alizarin red staining after osteogenic differentiation for 14 days. Scale bars are 200 μm. Osteogenic efficiencies were quantified by qPCR analysis of *Sp7* and *Bglap* expression (F) (n = 3 independent experiments).

Data information: The statistical significance of differences was analyzed by one-way ANOVAs with Tukey's multiple comparison tests. All data represented Mean ± SD. *P < 0.05, **P < 0.01.

labeled by both Cre lines, thereby justifying the use of Lepr-Cre to study SSCPs maintenance and lineage specification in adult long bones. The Prrx1-Cre-biased subsets, including periosteal cells, chondrocytes, and αSMA$^+$ cells, could be derived from perichondrial cells during embryonic skeletal development (Logan *et al*, 2002). In contrast, Lepr-Cre is not detected in long bones until perinatal stage (Zhou *et al*, 2014a), which could explain their distinct recombination patterns. Cautions must be taken that Lepr-Cre is a germline Cre that is not organ- or lineage specific. Since we could not temporally control the expression of Cre recombinase, Lepr-Cre might be ectopically induced upon certain stress conditions. Thus, careful analysis of *Lepr* expression is needed when inferring lineage relationships among different cell types traced by Lepr-Cre. Notably, a recent lineage tracing study by LepR-CreER reveals the transition of postnatal skeletal progenitor cells from chondrocytes to LepR$^+$ BMSCs (Shu *et al*, 2021). Future studies are needed to test the cellular heterogeneity within Lepr-CreER-traced cells in the adult long bones.

Integrated analysis of Prrx1-Cre- and Lepr-Cre-traced cells allowed us to systemically examine the distribution of known SSPC markers, as well as the extent to which different HSC niche cells overlap (Fig EV1E). Lepr-Cre$^+$ BMSCs expressed high levels of *Pdgfra*, *Pdgfrb*, *Kitl*, *Cxcl12,* and *Grem1*, which confirmed that they overlap with CAR cells (Omatsu *et al*, 2010) and Grem1$^+$ cells (Worthley *et al*, 2015). Previous studies showed that Lepr-Cre$^+$ BMSCs largely overlap with HSC niche-forming Nestin-GFP$^+$ cells, especially Nestin-GFP^{low} cells (Mendez-Ferrer *et al*, 2010; Kunisaki *et al*, 2013; Zhou *et al*, 2014a). Interestingly, *Nestin* and *CD105* were expressed in a smaller fraction of Lepr-Cre$^+$ BMSCs, which could be caused by sparse sampling by scRNA-seq, or by the heterogeneity within Lepr-Cre$^+$ BMSCs. Therefore, cautions must be taken when interpreting the expressional data reported in this study. We were not able to determine the relationship between Lepr-Cre$^+$ BMSCs and non-myelinating Schwann cells that were also implicated as critical HSC niche (Yamazaki *et al*, 2011), since these rare glial cells are derived from neural crest cells that could not be traced by Prrx1-Cre or Lepr-Cre.

Integrated analysis of Lepr-Cre-traced cells under homeostatic and stress conditions revealed adipogenic, osteogenic, and periosteal lineage cells. The adipogenic lineage cells are mainly composed of Lepr-Cre$^+$ BMSCs highly expressing HSC niche factors such as *Kitl* and *Cxcl12*, which were significantly down-regulated in aged, rosiglitazone-fed, and fractured mice, suggesting loss of the ability to create HSC niche. Importantly, we identified a slow cycling Notch3$^+$ sub-population within Lepr-Cre$^+$ BMSCs, which correspond to adventitial cells closely associated with the bone marrow

vasculatures, reminiscent of the quiescent Cxcl12-CreER$^+$ BMSCs in the perivascular region (Matsushita *et al*, 2020). Interestingly, Notch signaling has been previously shown to promote SSPC maintenance by suppressing osteogenic differentiation (Engin *et al*, 2008; Hilton *et al*, 2008). Conditional deletion of the Notch ligand *Dll4* in bone marrow ECs leads to myeloid skewing of hematopoietic progenitors (Tikhonova *et al*, 2019), significantly shorter long bones, and loss of trabeculae (Ramasamy *et al*, 2014). Together with our findings, these data indicate that bone marrow ECs create a vascular niche for SSPCs via the Dll-Notch axis, and play critical roles in orchestrating osteogenesis and hematopoiesis. Notably, the Notch3$^+$ subpopulation expresses a panel of angiogenic factors such as Vegfa and Col4a1, highlighting the intimate crosstalk between adventitial cells and bone marrow ECs. Future studies are needed to test whether different types of bone marrow ECs, including sinusoidal, arteriolar, and arterial ECs, constitute distinct niches for SSPC to regulate their self-renewal and lineage commitment.

Lepr-Cre$^+$ cells have been extensively studied in the bone marrow, while their periosteal functions remain largely unknown. Although *Lepr-Cre* labeled a small fraction of periosteal cells under steady state, they were expanded after bone fracture and irradiation, suggesting potential roles in skeletal repair in response to physical insults. Notably, since *Lepr-Cre* labels cells in the bone marrow, endosteal, and periosteal compartments, we could not rule out the possibility that bone marrow and endosteal Lepr-Cre$^+$ cells also give rise to chondrocytes after bone fracture (Fig 2G). In this study, we focused on the Sca-1$^+$ sub-population in both Lepr-Cre$^+$ and Lepr-Cre$^-$ fractions of the periosteum, which enriches CFU-F activity and exhibits adipogenic progenitor characteristics. This contrasts sharply with bone marrow PαS cells that exhibit trilineage differentiation potential (Morikawa *et al*, 2009), suggesting functional divergence of Sca-1$^+$ cells isolated from different skeletal compartments. On the contrary, Sca-1$^-$ periosteal cells seem to enrich SSPCs including PSCs (Debnath *et al*, 2018; cluster 3 in Fig EV5B, CD200$^+$CD105$^-$Thy1$^-$6C3$^-$) and αSMA$^+$ p-SSCs (Ortinau *et al*, 2019; cluster 2 in Fig 5B, expressing *Acta2*). Consistent with our findings (Fig 6), Ambrosi *et al* found that CD45$^-$CD31$^-$Sca1$^+$ cells enrich adipogenic progenitors, while CD45$^-$CD31$^-$Sca1$^-$ cells enrich osteochondrogenic progenitors (Ambrosi *et al*, 2017). Given that crushed bones containing both bone marrow and bone fragments were analyzed (Ambrosi *et al*, 2017), and that *Ly6a* (*Sca-1*) is expressed at a much higher level in periosteal/fibroblast populations as compared to BMSCs (Fig EV1E; Baryawno *et al*, 2019; Sivaraj *et al*, 2021), the CD45$^-$CD31$^-$Sca1$^+$ cells studied by Ambrosi *et al* might overlap, as least in part, with the Sca-1$^+$ periosteal cells that we analyzed.

Materials and Methods

Reagents and Tools table

Reagent/Resource	Reference or Source	Identifier or Catalog Number
Experimental Models		
Prrx1-Cre	Logan *et al* (2002)	JAX: 005584
Lepr-Cre	DeFalco *et al* (2001)	JAX: 008320
Loxp-STOP-loxp-tdTomato	Madisen *et al* (2010)	JAX: 007914
Col2.3-GFP	Kalajzic *et al* (2002)	JAX: 013134
Recombinant DNA		
pLKO.1 - TRC Cloning Vector	Addgene	Cat# 10878
pLKO.1_Hoxb2_1	This study	
pLKO.1_Hoxb2_2	This study	
pLKO.1_Npdc1_1	This study	
pLKO.1_Npdc1_2	This study	
Antibodies		
Anti-CD45-APC (Clone 30-F11)	eBioscience	Cat# 17-0451-83
Anti-Ter119-APC (Clone TER-119)	eBioscience	Cat# 17-5921-82
Anti-Tie2-APC (Clone TEK4)	Biolegend	Cat# 124010
Anti-Pdgfra-Biotin Antibody (Clone APA5)	eBioscience	Cat# 13-1401-82
Anti-Notch 3 Armenian Hamster Monoclonal Antibody (Clone HMN3-133)	Biolegend	Cat# 130512
Anti-Ly-6A/E (Sca-1)-PerCP/Cy5.5 (Clone E13-161.7)	Biolegend	Cat# 122524
FITC anti-BrdU Antibody (Clone 3D4)	Biolegend	Cat# 364104
Anti-CD31-biotin (Clone MEC13.3)	Biolegend	Cat# 102504
Mouse/Rat CD31/PECAM-1 Antibody	R&D system	Cat# AF3628-SP
Anti-Ly-6A/E-Alexa Fluor 647 (Clone E13-16.7)	Biolegend	Cat# 122518

Reagents and Tools table (continued)

Reagent/Resource	Reference or Source	Identifier or Catalog Number
Rabbit anti-Aggrecan Antibody	Millipore	Cat# AB1031
Rabbit anti-Perilipin Antibody	Sigma	Cat# P1873
Donkey anti-rabbit-Alexa Fluor 488	Invitrogen	Cat# A21206
Donkey anti-goat-Alexa Fluor 488	Invitrogen	Cat# A-11055
Donkey anti-rabbit-Alexa Fluor 647	Invitrogen	Cat# A-31573
Oligonucleotides and other sequence-based reagents		
Acan (NM_007424.2)	This study	qPCR primers
F: TGA AGC AGA AGG TCT GGA CA		
R: CCA GAA GGA ATC CCA CTA ACA		
Col2a1 (NM_031163.3)	This study	qPCR primers
F: GTC CCC CTG GCC TTA GTG		
R: CCA CCA GCC TTC TCG TCA		
Adipoq (NM_001310597.1)	This study	qPCR primers
F: TGT TCC TCT TAA TCC TGC CCA		
R: CCA ACC TGC ACA AGT TCC CTT		
Pparg (NM_011146.3)	This study	qPCR primers
F: ACC ACT CGC ATT CCT TTG AC		
R: TGG GTC AGC TCT TGT GAA TG		
Sp7 (NM_001348205.1)	This study	qPCR primers
F: CAA GAG TGA GCT GGC CTG A		
R: TGG AGC CAT AGT GAG CTT CTT		
Bglap (NM_007541.3)	This study	qPCR primers
F: TGA GGA CCA TCT TTC TGC TCA		
R: TGG ACA TGA AGG CTT TGT CA		
Hoxb2 (NM_134032.2)	This study	qPCR primers
F: CGA GGT CGG ATC ACC ATC		
R: GGT ACT TAT TGA AGT GGA ACT CCT TCT		
Npdc1 (NM_008721.4)	This study	qPCR primers
F: GTG CCA AGG AAA CA CTA TCTT		
R: CTC CTT CAG TGC CAG TTC CT		
ShRNA_Hoxb2_1	This study	shRNA-sequence
CCGGGTCTGGTCCTCCTTGGCTGTTCTCGAGAACAGCCAAGGAGGACCAGACTTTTTG		
ShRNA_Hoxb2_2	This study	shRNA-sequence
AATTCAAAAAGCCTTCTCCACTCGTGGATACCTCGAGGTATCCACGAGTGGAGAAGGC		
ShRNA_Npdc1_1	This study	shRNA-sequence
AATTCAAAAAGCTTTCTGCTTAGCAAGCTCACTCGAGTGAGCTTGCTAAGCAGAAAGC		
ShRNA_Npdc1_2	This study	shRNA-sequence
AATTCAAAAAGGCATAAGGAACCTCCAAAGGCTCGAGCCTTTGGAGGTTCCTTATGCC		
Chemicals, Enzymes and other reagents		
Anti-Biotin Microbeads	Miltenyi Biotec	Cat# 130-090-485
LS Columns	Miltenyi Biotec	Cat# 130-042-401
Type I Collagenase	Worthington	Cat# LS004197
Dispase II	Sigma-Aldrich	Cat# 04942078001
DNase I	Sigma-Aldrich	Cat# D4527-200KU
GelMA	Engineering for Life	EFL-GM-90

Reagents and Tools table (continued)

Reagent/Resource	Reference or Source	Identifier or Catalog Number
Sodium pyruvate solution	Gibco	Cat# S8636
Bovine serum albumin (BSA)	Sigma-Aldrich	Cat# A9647
Fetal bovine serum (FBS)	HyClone	Cat# SH30070.03
MEM alpha medium	Thermo Fisher Scientific	Cat# 12561-056
Penicillin-Streptomycin Solution	Thermo Fisher Scientific	Cat# 15140-122
LM-DMEM	Corning	Cat# 10-014-CV
DMEM with 4.5 g/l glucose L-glutamine & sodium pyruvate	Corning	Car# 10-013-CVR
L-Ascorbic acid 2-phosphate sesquimagnesium salt hydrate, ≥95%	Sigma-Aldrich	Cat# A8960-5G
L-proline	Sigma-Aldrich	Cat# P0380
Recombinant human TGF-b3	PeproTech	Cat# 100-36E
Indomethacin	Sigma-Aldrich	Cat# I7378
Alizarin Red S	Sigma-Aldrich	Cat# A5533
Oil Red O solution	Sigma-Aldrich	Cat# O1391
Alcian blue 8GX	Sangon Biotech	Cat# A600298-0001
Crystal Violet	Solarbio	Cat# C8470
5X All-In-One MasterMix Kit	ABM	Cat# G492
APC BrdU Flow Kit	BD Bioscience	Cat# 552598
5-Bromo-2′-deoxyuridine ≥ 99% (HPLC)	Sigma-Aldrich	Cat# B5002-5G
RQ1 RNase-Free Dnase,	Promega,	Cat# M6101
Matrigel	Corning	Cat# 354234
Chromium Single Cell 3' Library and Gel Bead Kit V2	10× Genomics	Cat# PN-120237
Chromium Next GEM Single Cell 3' GEM, Library & Gel Bead Kit V3.1	10× Genomics	Cat# 1000128
iTaq Universal SYBR Green Supermix	BioRad	Cat# 172-5125
Software		
Zen 2.3 software	Zeiss	
FlowJo V10.1	FlowJo LLC	https://www.flowjo.com/ solutions/flowjo
GraphPad Prism 7.0	GraphPad	https://www.graphpad.com/
Image J: Fiji	Image J	https://imagej.nih.gov/ij/
Snapgene V2.3.2	Snapgene	https://www.snapgene.com
Cell Ranger v3.0.1	10× Genomics	https://support.10xgenomics.com
Python 3	N/A	www.python.org
R 3.5.0	R-Project	https://cran.r-project.org/ mirrors.html
Seurat v2.3.4	Satija *et al* (2015)	https://satijalab.org/seurat/
Scanpy v1.4	Wolf *et al* (2018)	https://github.com/theislab/scanp
SCENIC	Aibar *et al* (2017)	https://github.com/aertslab/SCENIC
jvenn	Bardou *et al* (2014)	http://jvenn.toulouse.inra.fr/app/example.html
ClusterProfiler v3.2.14	Yu *et al* (2012)	https://guangchuangyu.github.io/software/ clusterProfiler/
TACS	Kernfeld *et al* (2018)	N/A
CellphoneDB v2.0.0	Vieira Braga *et al* (2019)	www.cellphonedb.org
Cytoscape v3.6	Otasek *et al* (2019)	www.cytoscape.org
GSEA v2.2.4	Subramanian *et al* (2005), Mootha *et al* (2003)	www.software.broadinstitute.org/gsea/, https://www.gsea-msigdb.org/gsea/index.jsp

Methods and Protocols

Mice

All mice were maintained in C57BL/6 background, including *Lepr-Cre* (DeFalco *et al*, 2001), *Prrx1-Cre* (Logan *et al*, 2002), *loxp-STOP-loxp-tdTomato* (Madisen *et al*, 2010), and *Col2.3-GFP* mice (Kalajzic *et al*, 2002). For scRNA-seq experiments in *Prrx1-Cre; tdTomato; Col2.3-GFP mice*, 8-week-old mice were analyzed (three males). For scRNA-seq experiments in *Lepr-Cre; tdTomato* mice, 8-week-old mice ("Young adult," four males and two females), 12-month-old mice ("Aging," four females), 10-week-old mice on 20 g/kg rosiglitazone-containing chow for 5 weeks ("Rosiglitazone diet," feeding started at 5 weeks old, two females), 8-week-old sub-lethally irradiated (5 Gy) mice ("Irradiation," two males and two females), and 8-week-old fractured mice ("Fracture," two males and two females) were analyzed. All mice were kept in an SPF facility operated in a 12-h light/dark cycle. Animal procedures were approved by the Tongji University Animal Care and Use Committee. No statistical methods were used to estimate sample size. Mice were randomly chosen for each sample, and blinding of the investigator was not considered in this study.

Immunofluorescent staining

Freshly dissected bones were fixed in 4% paraformaldehyde overnight at 4°C, decalcified in 10% EDTA for 3 days, and sectioned at 10 μm using the CryoJane Tape-Transfer system (Leica). Sections were blocked in PBS with 10% horse serum and 0.1% Triton X-100 at room temperature for 1 h, and stained overnight at 4°C with rabbit anti-Aggrecan (Millipore, AB1031 1:200), rabbit anti-Perilipin (Sigma, 1:1,000) rabbit-anti-Col2a1 (Boster, BA0533, 1:200), rabbit-anti-Sp7 (Abcam, ab209484, 1:200), or goat anti-CD31 (R&D systems, AF3628-SP, 1:200) primary antibodies. Sections were washed three times (10 min/each) at room temperature, and stained with anti-Ly-6A/E-Alexa Fluor 647 (Biolegend, clone: E13-161.7, 1:50), anti-Notch3-Alexa Fluor 647 (Biolegend, clone: HMN3-133, 1:100), donkey anti-rabbit-Alexa Fluor 488, anti-goat-Alexa Fluor 488, or donkey anti-rabbit-Alexa Fluor 647 antibodies (Invitrogen, 1:500) at room temperature for 1 h. Slides were mounted with Antifade Prolong Gold with DAPI (Invitrogen). Images were acquired with an Olympus IX73 fluorescent microscope. For immunostaining of the 3D coculture system, the GelMA hydrogels were treated as described above at 4°C during the whole process. Blocking, primary, and secondary antibody application were each performed overnight, and the washing time was extended to 30 min/each. Images were acquired with Zeiss LSM8800 confocal microscope and z-stack images were analyzed using Zen 2.3 software.

Bone fracture

After anesthesia, an incision was made on the skin of the right leg to expose the femur through the muscles. A stainless-steel wire was inserted into the intramedullary canal through the knee, and an incision was made by the cranial drill in the mid-diaphysis to introduce a fracture. The muscle and skin were then closed by sutures and wound clips. Mice were closely monitored until they resumed full activity. Ketoprofen was given for analgesia before and after surgery.

Enzymatic dissociation and flow cytometry

Enzymatic digestion of the bone and bone marrow cells were performed as previously described (Suire *et al*, 2012; Yue *et al*, 2016). Briefly, intact marrow plugs were flushed from the limb bones and subjected to two rounds of enzymatic digestion at 37°C for 15 min each. The remaining bone fragments were crushed and digested in the same ways as the marrow plugs. The digestion buffer contained 3 mg/ml type I collagenase (Worthington), 4 mg/ml Dispase (Sigma), and 1 U/ml DNase I (Ambion) in HBSS with calcium and magnesium. The cells were resuspended in staining medium (HBSS + 2% fetal bovine serum) with 2 mM EDTA to stop the digestion. The bone and marrow fractions were combined and filtered through 70-μm cell strainers before sorting. Fractured femurs were dissected and crushed for enzymatic digestion without flushing the marrows. To isolate periosteal cells for flow cytometry and functional analyses, long bones with periosteum were digested twice at 37°C for 15 min each. The loosened periosteum was scraped off with a razor blade and digested twice at 37°C for 15 min each. For flow cytometry, digested cells were stained with anti-CD45-APC (eBioscience, clone: 30-F11, 1:200), anti-Ter119-APC (eBioscience, clone TER-119, 1:200), and anti-Tie2-APC (Biolegend, clone: TEK4, 1:200) antibodies in staining buffer for 30 min on ice, washed and resuspended in 1 ml staining buffer with 1 μg/ml DAPI (Invitrogen). Cell sorting was performed on FACSAriaII flow cytometer (BD Biosciences) with a 100-μm nozzle, and sorted cells were collected in PBS supplemented with 0.08% UltraPure BSA in 96-well clear round bottom ultra-low attachment microplates (Corning 7007). When analyzing Lepr-Cre^{+}Sca-1$^{+/-}$ cells, anti-Ly-6A/E (Sca-1)-PerCP/Cy5.5 (Biolegend, clone: E13-161.7, 1:100) was used in combination with the above antibodies.

CFU-F culture and *in vitro* differentiation

To form CFU-F colonies, flow cytometrically sorted cells were plated in six-well plates (200 cells/well) with BMSC medium containing α-MEM (Gibco), 20% fetal bovine serum (FBS, Gibco 10270-106, Lot #: 42F6480K, selected to support CFU-F growth), 10 μM ROCK inhibitor, 1 mM sodium pyruvate, and 1% penicillin/streptomycin. Cultures were maintained at 37°C with 5% O_2 and 5% CO_2 to create a low oxygen environment that promoted cell survival and proliferation (Morrison *et al*, 2000). The culture medium was changed every 4 days. CFU-F colonies were counted 8 days after plating by crystal violet staining (1% in formalin solution). Adipogenic and osteogenic differentiation was assessed by replating primary CFU-F colonies into 24-well plates ($4–6 \times 10^4$ cells/cm^2). The adipogenic differentiation medium contained DMEM (Gibco), 10% fetal bovine serum, 0.5 μM isobutylmethylxanthine, 60 μM indomethacin, 1% penicillin/ streptomycin, 5 μg/ml insulin, and 1 μM dexamethasone. The medium was changed every 3–4 days, and the differentiation efficiency was determined by oil red O staining on day 7. The osteogenic differentiation medium contained α-MEM (Gibco), 10% fetal bovine serum (Gibco 10270-106, Lot #: 42F6480K, selected to support CFU-F growth), 1 mM sodium pyruvate, 1% penicillin/streptomycin, 50 μg/ml L-ascorbic acid, 10 mM β-glycerophosphate, and 100 nM dexamethasone. The medium was changed every 3–4 days, and the differentiation efficiency was determined by alizarin red staining on day 14. The chondrogenic medium contained 10 ng/ml recombinant transforming growth factor-b3 (Peprotech), 100 nM dexamethasone, 50 μg/ml ascorbic acid 2-phosphate, 1 mM sodium pyruvate, 40 μg/ml proline, 1% penicillin/streptomycin, and 1X ITS cell culture supplement (Cyagen) containing 6.25 μg/ml bovine insulin, 6.25 μg/ml transferrin, 6.25 μg/ml selenous acid, 5.33 μg/ml linoleic acid, and 1.25 mg/ml

BSA in high glucose DMEM. To form cell pellets, 2.5×10^5 cells were centrifuged in 15-ml polypropylene tubes. The medium was changed every 2 days in the first week, and then once a week. The differentiation efficiency was determined by cryosection of the cell pellets and alcian blue staining on day 21.

BrdU incorporation assay

For cell cycle analysis *in vivo*, 8-week-old *Lepr-Cre; tdTomato* mice were given a single intraperitoneal injection of BrdU (100 mg/kg body mass) and maintained on 0.5 mg/ml of BrdU in the drinking water for 14 days. For cell cycle analysis during *ex vivo* 3D co-culture, BrdU was administered at a final concentration of 10 μM from day 1 to day 5. The frequency of $BrdU^+$ cells was analyzed by flow cytometry using the BrdU Flow Kit (BD Biosciences) and FITC anti-BrdU Antibody (Biolegend, clone: 3D4, 1:100).

Ex vivo 3D co-culture

Primary BMSCs and bone marrow ECs were isolated from 8-week-old wild-type (for RNA-seq) or Lepr-Cre; tdTomato (for immunostaining) mice. Bone marrow plugs were flushed out of the limb bones and digested as described above. For 2D expansion of BMSCs, whole bone marrow cells were cultured at a density of 8×10^6 per 10-cm dish with BMSC medium for 8 days. For 2D expansion of bone marrow ECs, $CD31^+$ cells were immunomagnetically enriched from digested whole bone marrow cells using anti-CD31-biotin (Biolegend, clone: MEC13.3, 1:200) antibody, anti-Biotin MicroBeads (Miltenyi Biotech, 130-090-485), and MACS LS column (Miltenyi Biotech, 130-042-401). The enriched $CD31^+$ cells were cultured at a density of 2×10^7 cells per 10 cm fibronectin (Sigma, F0895) pre-coated dish with EGM2 medium (Lonza, CC-3202) for 8 days. 2D expanded BMSCs and bone marrow ECs were then purified by flow cytometry using anti-CD45-APC, anti-Ter119-APC, anti-CD140a-biotin (eBioscience, clone: APA5, 1:200), and anti-CD31-biotin antibodies. Ten thousand BMSCs and bone marrow ECs were mixed at 1:1 ratio in 50 μl GelMA (4%, Engineering for Life, GM-60) in a 24-well culture plate, and cross-linked with a 405-nm light source for 25 s to form hydrogel. 3D hydrogels were cultured in 500 μl EGM2 medium (changed once after 2–3 days) and maintained at 37°C with 5% O_2 and 5% CO_2 for 5 days.

Lentiviral transfection

Short hairpin RNAs (shRNA) targeting Hoxb2 and Npdc1 were cloned into pLKO.1 vector. HEK293T cells (2×10^5) were seeded in a six-well plate and transfected with pLKO.1-Hoxb2-shRNA, pLKO.1-Npdc1-shRNA, or pLKO.1 vector (control) together with packaging vectors (pAX2 and VSV-G) by PEI (Polysciences, 23966-1) for 8 h. The lentivirus-containing culture medium was harvested at 48 and 72 h post-transfection and stored at −80°C. For lentiviral transfection of BMSCs, 2×10^4 $Lepr\text{-}Cre^+$ BMSCs were seeded in a six-well plate and transfected with the lentivirus-containing medium (1:10 volume ratio). Cells were expanded after 48 h for *in vitro* differentiation and qPCR analyses.

Renal sub-capsular transplantation

Briefly, 2×0^5 cells were resuspended in 5 μl Matrigel (Corning, 354234) on ice and then aspirated into a micropipette (Drummond Scientific, 5-000-2010). The cell mixture was transplanted underneath the renal capsule of 7–8-week-old wild-type mice. Four weeks after transplantation, the kidneys were surgically removed, fixed in 4% paraformaldehyde for 6 h at 4°C, decalcified in 10% EDTA for 2 days, and then dehydrated in 30% sucrose at room temperature. Cryosections were cut at 10 μm and subjected to immunofluorescent staining, followed by Movat's Pentachrome staining (ScyTek, MPS-1). Images were acquired using Olympus IX73 microscope.

RNA extraction and qPCR

Total RNAs were extracted by RNAiso Plus (Takara) and reverse transcribed into cDNA using 5X All-In-One MasterMix kit (ABM). qPCR was performed using iTaq Universal SYBR Green Supermix (BioRad) on a CFX96 real-time system (BioRad).

scRNA-seq library preparation and sequencing

Flow cytometry-sorted cells were examined under a microscope, counted with a hemocytometer, and then subjected to 3' scRNA-seq library construction on a Chromium Controller (10× Genomics). All libraries were constructed with Single Cell 3' v2 kit according to the manufacturer's instructions except for the irradiation sample of female mice (Single Cell 3' v3 kit). Our target output was 4,000 cells for each sample. Reverse transcription, cDNA amplification, and library constructions were performed on T100 Touch Thermal cycler (Bio-Rad). Amplified cDNA and libraries were evaluated on an Agilent Tape-Station system using D5000 and D1000 screentapes (Agilent Technologies) and diluted to 10 ng/μl. Pooled samples were sequenced on a HiSeq X Ten system (Illumina) as paired-end 150-bp reads, to ~90% saturation level for all samples.

Pre-processing of scRNA-seq data

Paired-end sequencing reads were processed using the Cell Ranger pipelines (version 3.0, 10× Genomics) for sample demultiplexing, read mapping (mm10/GRCm38), barcode processing, and single-cell transcript counting. After removing poorly mapped reads and PCR duplicates, reads with valid cell barcodes and unique molecular identifiers (UMIs) were used to generate the gene-barcode matrix. To remove low-quality and contaminating hematopoietic cells, we excluded the following cells: (i) cells with fewer than 500 detected genes (each gene must have at least one UMI aligned); (ii) cells with more than 15% mitochondrial transcripts (UMIs); (iii) cells with more than 2% hemoglobin transcripts (UMIs) including *Hbb-bt, Hbb-bs, Hbb-bh1, Hbb-bh2, Hbb-y*; (iv) contaminating endothelial cells. After filtering, gene expression in each cell was calculated as transcripts per 10k transcripts (TP10K), representing the fraction of each gene's UMI count with respect to total UMIs in the cell and multiplied by 10,000. Only genes expressed in at least three cells were retained. The resulting digital expression matrix was log-transformed before downstream analyses. Detailed sample and single-cell information was listed in Dataset EV1.

Dimensionality reduction, clustering, and visualization

We performed dimensionality reduction and clustering using the Seurat package (v3.0.1) (Macosko *et al*, 2015). Briefly, we first selected a subset of highly variable genes based on dispersion of binned variance to mean expression ratios using the *FindVariableFeatures* function (with the MeanVarPlot method, $0.1 < \text{mean} < 8$, $\text{dispersion} > 1$) followed by filtering of dissociation artifact genes (van den Brink *et al*, 2017) and mitochondrial genes. We then performed principal component analysis (PCA) and

reduced the data to the top PCs (number of top PCs was chosen based on the "knee" point at the cumulative curve of standard deviations of each PCs). The PCA-reduced data were then used to compute a shared nearest neighbor graph, and were further subjected to graph-based clustering with the Louvain Method (Vincent D Blondel, 2008). The clusters were visualized on a two-dimensional t-distributed stochastic neighbor embedding (t-SNE) map (van der Maaten & Hinton, 2008), implemented by the Seurat software with perplexity = 30. Cell clustering is not driven by the cell cycle state except for cluster 6 in Fig 2C.

Batch effect correction

Batch effect correction was based on the assumption that different samples share similar subsets. Successfully batch correction was determined by overlapping of the same subsets from different samples. To correct batch effects, we used the Seurat alignment method for data integration. Briefly, we identified highly variable genes for each dataset as described above, and took the union of these genes to run a canonical correlation analysis to determine the common sources of variation among datasets by FindIntegrationAnchors function with the dims = 30. We then used IntegrateData function to align the sub-spaces on the basis of the first 30 canonical correlation vectors, which generated a new dimensional reduction that was used for further analysis (Tikhonova *et al*, 2019). We integrated Prrx1-Cre- and Lepr-Cre-traced samples and clustered 7,220 cells into 9 subsets (Fig 1B). The 17,224 cells from *Lepr-Cre*-traced samples were clustered into 8 subsets (Fig 2B).

Marker gene identification

To identify marker genes that define individual clusters, we performed pairwise differential expression analyses using the *FindAllMarkers* function in Seurat with the MAST method (Finak *et al*, 2015) for statistical tests. Differentially expressed autosomal genes that were detected in at least 20% cells within the cluster and with a $\log_2$ fold change > 0.2 compared with all other clusters were considered to be marker genes. Detailed DEG information for all figures were listed in Dataset EV2.

Reconstructing cell development trajectories

To infer the developmental progression of cells in different clusters and to order them in pseudotime, we used the non-linear reconstruction algorithm DDRTree in the Monocle 2 package (v2.10.0) (Qiu *et al*, 2017). The differentially expressed genes of different clusters were used as the ordering genes for the trajectory reconstruction.

Single-cell gene regulatory network inference using SCENIC

We performed SCENIC analysis to predict single-cell gene regulatory networks by following the standard workflow (Aibar *et al*, 2017). The raw count expression matrix was loaded onto GENIE3 for building the initial co-expression gene regulatory networks (GRN). The regulon data were then analyzed based on TF motifs from mm10-tss-centered-10 kb (for mouse) database by RcisTarget (Imrichova *et al*, 2015). The regulon activity scores in single cells were calculated using AUCell (Holland *et al*, 2020). Detailed regulon information for all figures was listed in source data for Figs 4 and 5.

RNA velocity

The spliced and unspliced reads were quantified by velocyto (version 0.17.11) with mouse genome reference. The velocities of each gene were calculated following the proposed workflow of scVelo (version 0.2.2; Bergen *et al*, 2020) with the default parameter. The trajectories were visualized on Uniform Manifold Approximation and Projection (UMAP) (Becht *et al*, 2018; Fig 1G).

GO and KEGG pathway analysis

The DEGs in each cluster were used to perform GO and KEGG pathway enrichment analysis by clusterProfiler package (Yu *et al*, 2012). The significantly expressed genes of each cluster were used as input and ontology was set to BP (biological process). The enriched GO terms and pathways were filtered by setting *P*-value cutoff to 0.05. Simplify function was performed to select the most significantly enriched terms.

Bulk RNA-seq of 3D-cultured BMSCs

Ten thousand lived BMSCs 3D cultured alone or together with bone marrow ECs in 4% GelMA hydrogels were sorted by flow cytometry ($CD45^-Ter119^-CD31^-CD140a^+$). Total RNAs were extracted, digested with DNase I, and purified using RNAclean Kit (TIANGEN, DP412). RNA-seq libraries were constructed by a modified Smart-seq2 protocol (Zhou *et al*, 2016) and sequenced using Nova-seq (PE150). Adaptor sequences were removed using CutAdapt and trimmed reads shorter than 30 bp were discarded. Trimmed data were aligned to mouse reference genome mm10 using STAR (Dobin *et al*, 2013; unique mapping rate > 80%). HTseq-count (Anders *et al*, 2015) was used to count the number of reads mapped to each gene. Counts of genes were normalized and differentially expressed genes (DEGs, $P < 0.05$, fold-change > 1.35) were determined by the DESeq2 package (Love *et al*, 2014). GO and KEGG enrichment of DEGs was performed using clusterProfiler package (Yu *et al*, 2012). Top 2% GO terms and top 20 KEGG pathways with $P < 0.05$ were chosen. DEGs, GO terms, and KEGG pathways were visualized using ggplot2. Normalized gene counts for all samples were listed in Dataset EV3.

Statistical analysis

The statistical significance of differences was analyzed by two-tailed unpaired Student's *t*-tests, or one-way ANOVAs with Tukey's multiple comparison tests. Detailed statistical methods were specified in the figure legends. All data represented Mean ± SD. $*P < 0.05$, $**P < 0.01$, $***P < 0.001$.

Data availability

The scRNA-seq and bulk RNA-seq data reported in this study have been deposited to Gene Expression Omnibus (GEO) with the accession number GSE138689 (https://www.ncbi.nlm.nih.gov/geo/query/acc.cgi?acc=GSE138689). R scripts for data analysis are available upon request.

Expanded View for this article is available online.

Acknowledgments

This work was supported by grants from the National Key R&D Program on Stem Cell and Translational Research (2017YFA0106400, 2017YFC1001500,

2021YFA1100900), National Natural Science Foundation of China (91749124, 81772389, 82070108, 31871478, 32022023), Zhejiang Provincial Natural Science Foundation of China (LR18C060001), Fundamental Research Funds for the Central Universities (22120190149, 22120200411, kx0200020173386), and Peak Disciplines (Type IV) of Institutions of Higher Learning in Shanghai.

Author contributions

CM performed most mouse experiments. JG and LS performed most bioinformatic analyses. HW performed the bone fracture surgeries. JQ helped with the scRNA-seq experiments. XZ, DC, and Yiying Z. performed 3D co-culture experiment and bulk RNA-seq analysis. Yuxi S. performed renal sub-capsular transplantation. CZ, YX, and Yong Z. helped with bioinformatic analysis. Yao S. and LS critically read the manuscript. RY designed and interpreted all experiments and wrote the manuscript.

Conflict of interest

The authors declare that they have no conflict of interest.

References

Ackert-Bicknell CL, Shockley KR, Horton LG, Lecka-Czernik B, Churchill GA, Rosen CJ (2009) Strain-specific effects of rosiglitazone on bone mass, body composition, and serum insulin-like growth factor-I. *Endocrinology* 150: 1330 – 1340

Van Agtmael T, Bailey MA, Schlotzer-Schrehardt U, Craigie E, Jackson IJ, Brownstein DG, Megson IL, Mullins JJ (2010) Col4a1 mutation in mice causes defects in vascular function and low blood pressure associated with reduced red blood cell volume. *Hum Mol Genet* 19: 1119 – 1128

Aibar S, González-Blas CB, Moerman T, Huynh-Thu VA, Imrichova H, Hulselmans G, Rambow F, Marine J-C, Geurts P, Aerts J *et al* (2017) SCENIC: single-cell regulatory network inference and clustering. *Nat Methods* 14: 1083 – 1086

Ambrosi TH, Scialdone A, Graja A, Gohlke S, Jank A-M, Bocian C, Woelk L, Fan H, Logan DW, Schürmann A *et al* (2017) Adipocyte accumulation in the bone marrow during obesity and aging impairs stem cell-based hematopoietic and bone regeneration. *Cell Stem Cell* 20: 771 – 784

Anders S, Pyl PT, Huber W (2015) HTSeq–a Python framework to work with high-throughput sequencing data. *Bioinformatics* 31: 166 – 169

Arnold MA, Kim Y, Czubryt MP, Phan D, McAnally J, Qi X, Shelton JM, Richardson JA, Bassel-Duby R, Olson EN (2007) MEF2C transcription factor controls chondrocyte hypertrophy and bone development. *Dev Cell* 12: 377 – 389

Baccin C, Al-Sabah J, Velten L, Helbling PM, Grunschlager F, Hernandez-Malmierca P, Nombela-Arrieta C, Steinmetz LM, Trumpp A, Haas S (2020) Combined single-cell and spatial transcriptomics reveal the molecular, cellular and spatial bone marrow niche organization. *Nat Cell Biol* 22: 38 – 48

Baker EK, Taylor S, Gupte A, Chalk AM, Bhattacharya S, Green AC, Martin TJ, Strbenac D, Robinson MD, Purton LE *et al* (2015) Wnt inhibitory factor 1 (WIF1) is a marker of osteoblastic differentiation stage and is not silenced by DNA methylation in osteosarcoma. *Bone* 73: 223 – 232

Bardou P, Mariette J, Escudié F, Djemiel C, Klopp C (2014) jvenn: an interactive Venn diagram viewer. *BMC Bioinform* 15: 293

Baryawno N, Przybylski D, Kowalczyk MS, Kfoury Y, Severe N, Gustafsson K, Kokkaliaris KD, Mercier F, Tabaka M, Hofree M *et al* (2019) A Cellular Taxonomy of the Bone Marrow Stroma in Homeostasis and Leukemia. *Cell* 177: 1915 – 1932

Becht E, McInnes L, Healy J, Dutertre CA, Kwok IWH, Ng LG, Ginhoux F, Newell EW (2018) Dimensionality reduction for visualizing single-cell data using UMAP. *Nat Biotechnol* 37: 38 – 44

Bergen V, Lange M, Peidli S, Wolf FA, Theis FJ (2020) Generalizing RNA velocity to transient cell states through dynamical modeling. *Nat Biotechnol* 38: 1408 – 1414

Vincent D Blondel J-LG, Renaud Lambiotte and Etienne Lefebvre (2008) Fast unfolding of communities in large networks. *J Stat Mech Theory Exp* 10: arXiv:0803.0476

Breitbach M, Kimura K, Luis TC, Fuegemann CJ, Woll PS, Hesse M, Facchini R, Rieck S, Jobin K, Reinhardt J *et al* (2018) *In vivo* labeling by CD73 marks multipotent stromal cells and highlights endothelial heterogeneity in the bone marrow niche. *Cell Stem Cell* 22: 262 – 276

van den Brink SC, Sage F, Vertesy A, Spanjaard B, Peterson-Maduro J, Baron CS, Robin C, van Oudenaarden A (2017) Single-cell sequencing reveals dissociation-induced gene expression in tissue subpopulations. *Nat Methods* 14: 935 – 936

Chan CK, Chen CC, Luppen CA, Kim JB, DeBoer AT, Wei K, Helms JA, Kuo CJ, Kraft DL, Weissman IL (2009) Endochondral ossification is required for haematopoietic stem-cell niche formation. *Nature* 457: 490 – 494

Chan C, Seo E, Chen J, Lo D, McArdle A, Sinha R, Tevlin R, Seita J, Vincent-Tompkins J, Wearda T *et al* (2015) Identification and specification of the mouse skeletal stem cell. *Cell* 160: 285 – 298

Chan D, Cole WG, Chow CW, Mundlos S, Bateman JF (1995) A COL2A1 mutation in achondrogenesis type II results in the replacement of type II collagen by type I and III collagens in cartilage. *J Biol Chem* 270: 1747 – 1753

Chen Q, Liu Y, Jeong HW, Stehling M, Dinh VV, Zhou B, Adams RH (2019) Apelin(+) endothelial niche cells control hematopoiesis and mediate vascular regeneration after myeloablative injury. *Cell Stem Cell* 25: 768 – 783

Crane GM, Jeffery E, Morrison SJ (2017) Adult haematopoietic stem cell niches. *Nat Rev Immunol* 17: 573 – 590

Cserjesi P, Lilly B, Bryson L, Wang Y, Sassoon DA, Olson EN (1992) MHox: a mesodermally restricted homeodomain protein that binds an essential site in the muscle creatine kinase enhancer. *Development* 115: 1087 – 1101

Debnath S, Yallowitz AR, McCormick J, Lalani S, Zhang T, Xu R, Li NA, Liu Y, Yang YS, Eiseman M *et al* (2018) Discovery of a periosteal stem cell mediating intramembranous bone formation. *Nature* 562: 133 – 139

DeFalco J, Tomishima M, Liu H, Zhao C, Cai X, Marth JD, Enquist L, Friedman JM (2001) Virus-assisted mapping of neural inputs to a feeding center in the hypothalamus. *Science* 291: 2608 – 2613

Delgado-Calle J, Sanudo C, Sanchez-Verde L, Garcia-Renedo RJ, Arozamena J, Riancho JA (2011) Epigenetic regulation of alkaline phosphatase in human cells of the osteoblastic lineage. *Bone* 49: 830 – 838

Ding L, Saunders TL, Enikolopov G, Morrison SJ (2012) Endothelial and perivascular cells maintain haematopoietic stem cells. *Nature* 481: 457 – 462

Dobin A, Davis CA, Schlesinger F, Drenkow J, Zaleski C, Jha S, Batut P, Chaisson M, Gingeras TR (2013) STAR: ultrafast universal RNA-seq aligner. *Bioinformatics* 29: 15 – 21

Docheva D, Hunziker EB, Fassler R, Brandau O (2005) Tenomodulin is necessary for tenocyte proliferation and tendon maturation. *Mol Cell Biol* 25: 699 – 705

Doege KJ, Sasaki M, Kimura T, Yamada Y (1991) Complete coding sequence and deduced primary structure of the human cartilage large aggregating proteoglycan, aggrecan. Human-specific repeats, and additional alternatively spliced forms. *J Biol Chem* 266: 894 – 902

Domenga V, Fardoux P, Lacombe P, Monet M, Maciazek J, Krebs LT, Klonjkowski B, Berrou E, Mericskay M, Li Z *et al* (2004) Notch3 is required for arterial identity and maturation of vascular smooth muscle cells. *Genes Dev* 18: 2730 – 2735

Duchamp de Lageneste O, Julien A, Abou-Khalil R, Frangi G, Carvalho C, Cagnard N, Cordier C, Conway SJ, Colnot C (2018) Periosteum contains skeletal stem cells with high bone regenerative potential controlled by Periostin. *Nat Commun* 9: 773

Engin F, Yao Z, Yang T, Zhou G, Bertin T, Jiang MM, Chen Y, Wang L, Zheng H, Sutton RE *et al* (2008) Dimorphic effects of Notch signaling in bone homeostasis. *Nat Med* 14: 299 – 305

Farrell M, Fairfield H, Costa S, D'Amico A, Falank C, Brooks DJ, Reagan MR (2021) Sclerostin-neutralizing antibody treatment rescues negative effects of rosiglitazone on mouse bone parameters. *J Bone Miner Res* 36: 158 – 169

Finak G, McDavid A, Yajima M, Deng J, Gersuk V, Shalek AK, Slichter CK, Miller HW, McElrath MJ, Prlic M *et al* (2015) MAST: a flexible statistical framework for assessing transcriptional changes and characterizing heterogeneity in single-cell RNA sequencing data. *Genome Biol* 16: 278

Grčević D, Sironi M, Valentino S, Deban L, Cvija H, Inforzato A, Kovačić N, Katavić V, Kelava T, Kalajzić I *et al* (2018) The long pentraxin 3 plays a role in bone turnover and repair. *Front Immunol* 9: 417

Greenbaum A, Hsu YM, Day RB, Schuettpelz LG, Christopher MJ, Borgerding JN, Nagasawa T, Link DC (2013) CXCL12 in early mesenchymal progenitors is required for haematopoietic stem-cell maintenance. *Nature* 495: 227 – 230

Han X, Wang R, Zhou Y, Fei L, Sun H, Lai S, Saadatpour A, Zhou Z, Chen H, Ye F *et al* (2018) Mapping the mouse cell atlas by Microwell-seq. *Cell* 172: 1091 – 1107

Hilton MJ, Tu X, Wu X, Bai S, Zhao H, Kobayashi T, Kronenberg HM, Teitelbaum SL, Ross FP, Kopan R *et al* (2008) Notch signaling maintains bone marrow mesenchymal progenitors by suppressing osteoblast differentiation. *Nat Med* 14: 306 – 314

Holland CH, Tanevski J, Perales-Patón J, Gleixner J, Kumar MP, Mereu E, Joughin BA, Stegle O, Lauffenburger DA, Heyn H *et al* (2020) Robustness and applicability of transcription factor and pathway analysis tools on single-cell RNA-seq data. *Genome Biol* 21: 36

Horowitz MC, Berry R, Holtrup B, Sebo Z, Nelson T, Fretz JA, Lindskog D, Kaplan JL, Ables G, Rodeheffer MS *et al* (2017) Bone marrow adipocytes. *Adipocyte* 6: 193 – 204

Imrichova H, Hulselmans G, Atak ZK, Potier D, Aerts S (2015) i-cisTarget 2015 update: generalized cis-regulatory enrichment analysis in human, mouse and fly. *Nucleic Acids Res* 43: W57 – W64

Isern J, Garcia-Garcia A, Martin AM, Arranz L, Martin-Perez D, Torroja C, Sanchez-Cabo F, Mendez-Ferrer S (2014) The neural crest is a source of mesenchymal stem cells with specialized hematopoietic stem cell niche function. *Elife* 3: e03696

Kalajzic I, Kalajzic Z, Kaliterna M, Gronowicz G, Clark SH, Lichtler AC, Rowe D (2002) Use of type I collagen green fluorescent protein transgenes to identify subpopulations of cells at different stages of the osteoblast lineage. *J Bone Miner Res* 17: 15 – 25

Kernfeld EM, Genga RMJ, Neherin K, Magaletta ME, Xu P, Maehr R (2018) A single-cell transcriptomic atlas of thymus organogenesis resolves cell types and developmental maturation. *Immunity* 48: 1258 – 1270.e6

Kim JH, Kim K, Youn BU, Lee J, Kim I, Shin HI, Akiyama H, Choi Y, Kim N (2014) Kruppel-like factor 4 attenuates osteoblast formation, function, and cross talk with osteoclasts. *J Cell Biol* 204: 1063 – 1074

Kindblom JM, Gevers EF, Skrtic SM, Lindberg MK, Gothe S, Tornell J, Vennstrom B, Ohlsson C (2005) Increased adipogenesis in bone marrow but decreased bone mineral density in mice devoid of thyroid hormone receptors. *Bone* 36: 607 – 616

Koide Y, Morikawa S, Mabuchi YO, Muguruma Y, Hiratsu E, Hasegawa K, Kobayashi M, Ando K, Kinjo K, Okano H *et al* (2007) Two distinct stem cell lineages in murine bone marrow. *Stem Cells* 25: 1213 – 1221

Kratochwil K, Ghaffari-Tabrizi N, Holzinger I, Harbers K (1993) Restricted expression of Mov13 mutant alpha 1(I) collagen gene in osteoblasts and its consequences for bone development. *Dev Dyn* 198: 273 – 283

Kunisaki Y, Bruns I, Scheiermann C, Ahmed J, Pinho S, Zhang D, Mizoguchi T, Wei Q, Lucas D, Ito K *et al* (2013) Arteriolar niches maintain haematopoietic stem cell quiescence. *Nature* 502: 637 – 643

Li Y, Ge C, Franceschi RT (2010) Differentiation-dependent association of phosphorylated extracellular signal-regulated kinase with the chromatin of osteoblast-related genes. *J Bone Miner Res* 25: 154 – 163

Liu Y, Strecker S, Wang L, Kronenberg MS, Wang W, Rowe DW, Maye P (2013) Osterix-cre labeled progenitor cells contribute to the formation and maintenance of the bone marrow stroma. *PLoS One* 8: e71318

Logan M, Martin JF, Nagy A, Lobe C, Olson EN, Tabin CJ (2002) Expression of Cre recombinase in the developing mouse limb bud driven by a Prxl enhancer. *Genesis* 33: 77 – 80

Love MI, Huber W, Anders S (2014) Moderated estimation of fold change and dispersion for RNA-seq data with DESeq2. *Genome Biol* 15: 550

van der Maaten L, Hinton G (2008) Visualizing data using t-SNE. *J Mach Learn Res* 9: 2579 – 2605

Macosko E, Basu A, Satija R, Nemesh J, Shekhar K, Goldman M, Tirosh I, Bialas A, Kamitaki N, Martersteck E *et al* (2015) Highly parallel genome-wide expression profiling of individual cells using nanoliter droplets. *Cell* 161: 1202 – 1214

Madisen L, Zwingman TA, Sunkin SM, Oh SW, Zariwala HA, Gu H, Ng LL, Palmiter RD, Hawrylycz MJ, Jones AR *et al* (2010) A robust and high-throughput Cre reporting and characterization system for the whole mouse brain. *Nat Neurosci* 13: 133 – 140

Maes C, Kobayashi T, Selig MK, Torrekens S, Roth SI, Mackem S, Carmeliet G, Kronenberg HM (2010) Osteoblast precursors, but not mature osteoblasts, move into developing and fractured bones along with invading blood vessels. *Dev Cell* 19: 329 – 344

Matsushita Y, Nagata M, Kozloff KM, Welch JD, Mizuhashi K, Tokavanich N, Hallett SA, Link DC, Nagasawa T, Ono W *et al* (2020) A Wnt-mediated transformation of the bone marrow stromal cell identity orchestrates skeletal regeneration. *Nat Commun* 11: 332

Mendez-Ferrer S, Michurina TV, Ferraro F, Mazloom AR, Macarthur BD, Lira SA, Scadden DT, Ma'ayan A, Enikolopov GN, Frenette PS (2010) Mesenchymal and haematopoietic stem cells form a unique bone marrow niche. *Nature* 466: 829 – 834

Miraoui H, Severe N, Vaudin P, Pages JC, Marie PJ (2010) Molecular silencing of Twist1 enhances osteogenic differentiation of murine mesenchymal stem cells: implication of FGFR2 signaling. *J Cell Biochem* 110: 1147 – 1154

Mizoguchi T, Pinho S, Ahmed J, Kunisaki Y, Hanoun M, Mendelson A, Ono N, Kronenberg HM, Frenette PS (2014) Osterix marks distinct waves of primitive and definitive stromal progenitors during bone marrow development. *Dev Cell* 29: 340 – 349

Mootha VK, Lindgren CM, Eriksson KF, Subramanian A, Sihag S, Lehar J, Puigserver P, Carlsson E, Ridderstråle M, Laurila E *et al* (2003) PGC-1α-responsive genes involved in oxidative phosphorylation are coordinately downregulated in human diabetes. *Nat Genet* 34: 267 – 273

Morikawa S, Mabuchi YO, Kubota Y, Nagai Y, Niibe K, Hiratsu E, Suzuki S, Miyauchi-Hara C, Nagoshi N, Sunabori T *et al* (2009) Prospective identification, isolation, and systemic transplantation of multipotent

mesenchymal stem cells in murine bone marrow. *J Exp Med* 206: 2483 – 2496

Morrison SJ, Perez SE, Qiao Z, Verdi JM, Hicks C, Weinmaster G, Anderson DJ (2000) Transient Notch activation initiates an irreversible switch from neurogenesis to gliogenesis by neural crest stem cells. *Cell* 101: 499 – 510

Nagoshi N, Shibata S, Kubota Y, Nakamura M, Nagai Y, Satoh E, Morikawa S, Okada Y, Mabuchi YO, Katoh H *et al* (2008) Ontogeny and multipotency of neural crest-derived stem cells in mouse bone marrow, dorsal root ganglia, and whisker pad. *Cell Stem Cell* 2: 392 – 403

Omatsu Y, Sugiyama T, Kohara H, Kondoh G, Fujii N, Kohno K, Nagasawa T (2010) The essential functions of adipo-osteogenic progenitors as the hematopoietic stem and progenitor cell niche. *Immunity* 33: 387 – 399

Ono N, Ono W, Nagasawa T, Kronenberg HM (2014) A subset of chondrogenic cells provides early mesenchymal progenitors in growing bones. *Nat Cell Biol* 16: 1157 – 1167

Ortinau LC, Wang H, Lei K, Deveza L, Jeong Y, Hara Y, Grafe I, Rosenfeld SB, Lee D, Lee B *et al* (2019) Identification of functionally distinct Mx1+alphaSMA+ periosteal skeletal stem cells. *Cell Stem Cell* 25: 784 – 796

Otasek D, Morris JH, Bouças J, Pico AR, Demchak B (2019) Cytoscape automation: empowering workflow-based network analysis. *Genome Biol* 20: 185

Park D, Spencer JA, Koh BI, Kobayashi T, Fujisaki J, Clemens TL, Lin CP, Kronenberg HM, Scadden DT (2012) Endogenous bone marrow MSCs are dynamic, fate-restricted participants in bone maintenance and regeneration. *Cell Stem Cell* 10: 259 – 272

Pinho S, Lacombe J, Hanoun M, Mizoguchi T, Bruns I, Kunisaki Y, Frenette PS (2013) PDGFRalpha and CD51 mark human nestin+ sphere-forming mesenchymal stem cells capable of hematopoietic progenitor cell expansion. *J Exp Med* 210: 1351 – 1367

Qiu X, Mao Q, Tang Y, Wang L, Chawla R, Pliner HA, Trapnell C (2017) Reversed graph embedding resolves complex single-cell trajectories. *Nat Methods* 14: 979 – 982

Ramasamy SK, Kusumbe AP, Wang L, Adams RH (2014) Endothelial Notch activity promotes angiogenesis and osteogenesis in bone. *Nature* 507: 376 – 380

Rodeheffer MS, Birsoy K, Friedman JM (2008) Identification of white adipocyte progenitor cells in vivo. *Cell* 135: 240 – 249

Roy S, Khanna S, Rink T, Radtke J, Williams WT, Biswas S, Schnitt R, Strauch AR, Sen CK (2007) P21waf1/cip1/sdi1 as a central regulator of inducible smooth muscle actin expression and differentiation of cardiac fibroblasts to myofibroblasts. *Mol Biol Cell* 18: 4837 – 4846

Sacchetti B, Funari A, Michienzi S, Di Cesare S, Piersanti S, Saggio I, Tagliafico E, Ferrari S, Robey PG, Riminucci M *et al* (2007) Self-renewing osteoprogenitors in bone marrow sinusoids can organize a hematopoietic microenvironment. *Cell* 131: 324 – 336

Sadie-Van Gijsen H, Hough FS, Ferris WF (2013) Determinants of bone marrow adiposity: the modulation of peroxisome proliferator-activated receptor-gamma2 activity as a central mechanism. *Bone* 56: 255 – 265

Satija R, Farrell JA, Gennert D, Schier AF, Regev A (2015) Spatial reconstruction of single-cell gene expression data. *Nat Biotechnol* 33: 495 – 502

Seike M, Omatsu Y, Watanabe H, Kondoh G, Nagasawa T (2018) Stem cell niche-specific Ebf3 maintains the bone marrow cavity. *Genes Dev* 32: 359 – 372

Shu HS, Liu YL, Tang XT, Zhang XS, Zhou B, Zou W, Zhou BO (2021) Tracing the skeletal progenitor transition during postnatal bone formation. *Cell Stem Cell* 28: 2122 – 2136

Sivaraj KK, Jeong HW, Dharmalingam B, Zeuschner D, Adams S, Potente M, Adams RH (2021) Regional specialization and fate specification of bone stromal cells in skeletal development. *Cell Rep* 36: 109352

Skelly DA, Squiers GT, McLellan MA, Bolisetty MT, Robson P, Rosenthal NA, Pinto AR (2018) Single-cell transcriptional profiling reveals cellular diversity and intercommunication in the mouse heart. *Cell Rep* 22: 600 – 610

Subramanian A, Tamayo P, Mootha VK, Mukherjee S, Ebert BL, Gillette MA, Paulovich A, Pomeroy SL, Golub TR, Lander ES *et al* (2005) Gene set enrichment analysis: a knowledge-based approach for interpreting genome-wide expression profiles. *Proc Natl Acad Sci* 102: 15545 – 15550

Sugiyama T, Kohara H, Noda M, Nagasawa T (2006) Maintenance of the hematopoietic stem cell pool by CXCL12-CXCR4 chemokine signaling in bone marrow stromal cell niches. *Immunity* 25: 977 – 988

Suire C, Brouard N, Hirschi K, Simmons PJ (2012) Isolation of the stromal-vascular fraction of mouse bone marrow markedly enhances the yield of clonogenic stromal progenitors. *Blood* 119: e86 – e95

Takashima Y, Era T, Nakao K, Kondo S, Kasuga M, Smith AG, Nishikawa S (2007) Neuroepithelial cells supply an initial transient wave of MSC differentiation. *Cell* 129: 1377 – 1388

Tikhonova AN, Dolgalev I, Hu H, Sivaraj KK, Hoxha E, Cuesta-Domínguez Á, Pinho S, Akhmetzyanova I, Gao J, Witkowski M *et al* (2019) The bone marrow microenvironment at single-cell resolution. *Nature* 569: 222 – 228

Vieira Braga FA, Kar G, Berg M, Carpaij OA, Polanski K, Simon LM, Brouwer S, Gomes T, Hesse L, Jiang J *et al* (2019) A cellular census of human lungs identifies novel cell states in health and in asthma. *Nat Med* 25: 1153 – 1163

Wolf FA, Angerer P, Theis FJ (2018) SCANPY: large-scale single-cell gene expression data analysis. *Genome Biol* 19: 15

Worthley D, Churchill M, Compton J, Tailor Y, Rao M, Si Y, Levin D, Schwartz M, Uygur A, Hayakawa Y *et al* (2015) Gremlin 1 identifies a skeletal stem cell with bone, cartilage, and reticular stromal potential. *Cell* 160: 269 – 284

Yamazaki S, Ema H, Karlsson G, Yamaguchi T, Miyoshi H, Shioda S, Taketo MM, Karlsson S, Iwama A, Nakauchi H (2011) Nonmyelinating Schwann cells maintain hematopoietic stem cell hibernation in the bone marrow niche. *Cell* 147: 1146 – 1158

Yang L, Tsang KY, Tang HC, Chan D, Cheah KS (2014) Hypertrophic chondrocytes can become osteoblasts and osteocytes in endochondral bone formation. *Proc Natl Acad Sci USA* 111: 12097 – 12102

Yang X, Matsuda K, Bialek P, Jacquot S, Masuoka HC, Schinke T, Li L, Brancorsini S, Sassone-Corsi P, Townes TM *et al* (2004) ATF4 is a substrate of RSK2 and an essential regulator of osteoblast biology; implication for Coffin-Lowry Syndrome. *Cell* 117: 387 – 398

Yu G, Wang LG, Han Y, He QY (2012) clusterProfiler: an R package for comparing biological themes among gene clusters. *OMICS* 16: 284 – 287

Yue R, Zhou BO, Shimada IS, Zhao Z, Morrison SJ (2016) Leptin receptor promotes adipogenesis and reduces osteogenesis by regulating mesenchymal stromal cells in adult bone marrow. *Cell Stem Cell* 18: 782 – 796

Zhong L, Yao L, Tower RJ, Wei Y, Miao Z, Park J, Shrestha R, Wang L, Yu W, Holdreith N *et al* (2020) Single cell transcriptomics identifies a unique adipose lineage cell population that regulates bone marrow environment. *Elife* 9: e54695

Zhou BO, Yu H, Yue R, Zhao Z, Rios JJ, Naveiras O, Morrison SJ (2017) Bone marrow adipocytes promote the regeneration of stem cells and haematopoiesis by secreting SCF. *Nat Cell Biol* 19: 891 – 903

Zhou BO, Yue R, Murphy MM, Peyer JG, Morrison SJ (2014a) Leptin-receptor-expressing mesenchymal stromal cells represent the main source of bone formed by adult bone marrow. *Cell Stem Cell* 15: 154 – 168

Zhou F, Li X, Wang W, Zhu P, Zhou J, He W, Ding M, Xiong F, Zheng X, Li Z *et al* (2016) Tracing haematopoietic stem cell formation at single-cell resolution. *Nature* 533: 487 – 492

Zhou X, von der Mark K, Henry S, Norton W, Adams H, de Crombrugghe B (2014b) Chondrocytes transdifferentiate into osteoblasts in endochondral bone during development, postnatal growth and fracture healing in mice. *PLoS Genet* 10: e1004820